

The Millennium Galaxy Catalogue: a census of local compact galaxies

J. Liske,^{1*} S. P. Driver,² P. D. Allen,² N. J. G. Cross³ and R. De Propris^{4,5}

¹European Southern Observatory, Karl-Schwarzschild-Str. 2, 85748 Garching, Germany

²Research School of Astronomy & Astrophysics, Australian National University, Cotter Road, Weston, ACT 2611, Australia

³Institute for Astronomy, University of Edinburgh, Royal Observatory, Blackford Hill, Edinburgh EH9 3HJ

⁴H.H. Wills Physics Laboratory, University of Bristol, Tyndall Avenue, Bristol BS8 1TL

⁵Cerro Tololo Inter-American Observatory, Casilla 603, La Serena, Chile

Accepted Received

ABSTRACT

We use the Millennium Galaxy Catalogue (MGC) to study the effect of compact galaxies on the local field galaxy luminosity function. Here we observationally define as ‘compact’ galaxies that are too small to be *reliably* distinguished from stars using a standard star-galaxy separation technique. In particular, we estimate the fraction of galaxies that are misclassified as stars due to their compactness.

We have spectroscopically identified *all* objects to $B_{\text{MGC}} = 20$ mag in a 1.14 deg^2 sub-region of the MGC, regardless of morphology. From these data we develop a model of the high surface brightness incompleteness and estimate that ~ 1 per cent of galaxies with $B_{\text{MGC}} < 20$ mag are misclassified as stars, with an upper limit of 2.3 per cent at 95 per cent confidence. However, since the missing galaxies are preferentially sub- L^* their effect on the faint end of the luminosity function is substantially amplified: we find that they contribute ~ 6 per cent to the total luminosity function in the range $-17 < M_B < -14$ mag, which raises the faint end slope α by $0.03^{+0.02}_{-0.01}$. Their contribution to the total B -band luminosity density is ~ 2 per cent. Roughly half of the missing galaxies have already been recovered through spectroscopy of morphologically stellar targets selected mainly by colour. We find that the missing galaxies mostly consist of intrinsically small, blue, star-forming, sub- L^* objects.

In combination with the recent results of Driver et al. (2005) we have now demonstrated that the MGC is free from both high and low surface brightness selection bias for giant galaxies ($M_B \lesssim -17$ mag). Dwarf galaxies, on the other hand, are significantly affected by these selection effects. To gain a complete view of the dwarf population will require both deeper and higher resolution surveys.

Key words: surveys – galaxies: statistics – galaxies: fundamental parameters.

1 INTRODUCTION

The idea that galaxies at a given luminosity span a wide range in surface brightness (SB) and that selection effects might cause both high and low SB galaxies to be under-represented in the observed galaxy distribution goes back to at least Reaves (1956); Zwicky (1957); Arp (1965) and Disney (1976). Low SB galaxies are difficult to detect because of their low contrast against the sky (Impey & Bothun 1997) while high SB galaxies may be confused with stars. Previously overlooked types of galaxies have indeed been uncovered over time, such as the giant low SB galaxy Malin 1 (Bothun et al. 1987) and several types of blue compact galaxies (Zwicky 1966; see Kunth & Östlin 2000 for a recent review)

at various luminosities and redshifts, including H II galaxies (e.g. Sargent & Searle 1970; Telles et al. 1997), blue compact dwarfs (e.g. Thuan & Martin 1981; Cairós et al. 2001) and luminous compact blue galaxies (Phillips et al. 1997; Guzmán et al. 2003) which in turn include the compact narrow emission line galaxies (CNELGs) of Koo et al. (1994, 1995); Guzman et al. (1996, 1998). Most recently a potentially new class of faint and compact objects, the so-called ultra compact dwarfs (UCDs), was discovered in the Fornax (Hilker et al. 1999; Drinkwater et al. 2000, 2003; see also Mieske, Hilker & Infante 2004), Abell 1689 (Mieske et al. 2004) and Virgo clusters (Haşegan et al. 2005).

The extent to which a given survey misses these sorts of galaxies depends on the survey’s detailed selection limits in the luminosity–SB plane (LSP). These in turn are determined by the survey’s apparent magnitude, SB and size limits, i.e. by its depth

* E-mail: jliske@eso.org

and resolution. Recently, Driver et al. (2005) presented the bivariate brightness distribution of the Millennium Galaxy Catalogue (MGC; Liske et al. 2003), i.e. the space density of galaxies in the LSP. They used simulations to determine the MGC’s selection limits and found that the observed galaxy distribution was well separated from both the low and high SB selection limits for luminosities brighter than at least $M_B \approx -18$ mag (see their fig. 12). Hence SB selection effects are not a significant issue in the MGC at these luminosities (unless the SB distribution of galaxies is bimodal) and in that sense the bright end of MGC’s luminosity function (LF) is truly ‘global’. The goal is now to obtain a similarly complete picture at lower luminosities.

To probe the galaxies beyond the MGC’s *low* SB limit requires deeper imaging and spectroscopy on 8-m class telescopes.

In this paper we will instead address the question of what lies beyond the MGC’s *high* SB selection limit. In particular, what is the effect of the compact galaxies beyond this limit on the local field galaxy LF and what is their contribution to the luminosity density? To answer these questions we must first understand and quantify the MGC’s incompleteness due to some compact galaxies having been misclassified as stars from the imaging data. To this end we have assembled two datasets:

First, we conducted an all-object spectroscopic survey in the range $16 \leq B_{\text{MGC}} < 20$ mag over a 1.14 deg^2 sub-region of the MGC, targeting *all* detected objects in this magnitude range, regardless of classification, morphology, colour or any other properties. This complete sample will be used to determine the fraction of galaxies that have been misclassified due to their compact nature.

A few such all-object surveys have been performed previously: Morton, Krug & Tritton (1985) observed all 606 objects to $B \leq 20$ mag in a 0.31 deg^2 region while Colless et al. (1990, 1991) investigated a random sample of 266 objects in the range $21 \leq b_J \leq 23.5$ mag. Most recently, Drinkwater et al. (2000) described an ambitious project to observe 14 000 objects with $16.5 \leq b_J \leq 19.7$ mag in a 12 deg^2 region centered on the Fornax cluster, which led to the discovery of 13 compact galaxies behind the Fornax cluster (mostly CNELG-like objects but also including four redder, weaker emission line galaxies; Drinkwater et al. 1999) as well as the UCDs in the cluster itself mentioned above.

Unfortunately, these previous studies cannot be used to reliably and quantitatively predict the number of compact galaxies misclassified as stars by the MGC because they either lack SB measurements or were performed in a special environment. On the other hand, many studies concerning the known compact galaxy populations contain very detailed SB information but they do not use complete samples, and hence cannot be used to make precise predictions either.

The second dataset consists of all available spectroscopy of stellar objects in the range $16 \leq B_{\text{MGC}} < 20$ mag in the full MGC survey region. We have augmented existing public data (almost exclusively of QSO candidates) with observations of additional stellar objects. Although these data are incomplete they provide a lower limit on the frequency of misclassified compact galaxies and help in the investigation of their properties.

The paper is organised as follows: we describe our data in Section 2, study the properties of compact galaxies masquerading as stars in Section 3 and quantify the MGC’s incompleteness due to misclassification in Section 4. In Section 5 we evaluate the contribution of compact galaxies to the local galaxy luminosity function and density. Finally, we summarise our findings in Section 6. We use $H_0 = 100 h \text{ km s}^{-1} \text{ Mpc}^{-1}$, $\Omega_M = 0.3$ and $\Omega_\Lambda = 0.7$ throughout.

2 DATA

2.1 The MGC

The Millennium Galaxy Catalogue (MGC; Liske et al. 2003) is a deep ($\mu_{\text{LIM}} = 26 \text{ mag arcsec}^{-2}$, $B_{\text{LIM}} = 24$ mag), wide-field (37.5 deg^2) *B*-band imaging survey conducted with the Wide Field Camera on the 2.5-m Isaac Newton Telescope. The survey region is a 72-deg long, 35-arcmin wide strip along the equator, and is fully contained within the survey regions of the Sloan Digital Sky Survey (SDSS; York et al. 2000) and the 2dF Galaxy Redshift Survey (2dFGRS; Colless et al. 2001).

Details of the observations, reduction, object detection using SEXTRACTOR (Bertin & Arnouts 1996) and catalogue construction are given by Liske et al. (2003). As it pertains to the present investigation we briefly remind the reader of our star/galaxy separation procedure for objects with $16 \leq B_{\text{MGC}} < 20$ mag.

As a starting point for classification we used the stellarity parameter provided by SEXTRACTOR, which is produced for each object by an artificial neural network. Its input consists of nine object parameters (eight isophotal areas and the peak intensity) and the seeing. The output consists of a single number, called stellarity, which takes a value of 1 for unresolved objects, 0 for extended objects and intermediate values in more dubious cases. We began by classifying all objects with stellarity ≥ 0.98 as stellar. This is a ‘natural’ value to adopt because the stellarity distribution rises sharply from 0.97 to 0.98 (see fig. 9 of Liske et al. 2003). All remaining objects were then inspected visually and classified as stars, galaxies, asteroids (defined as apparently real objects without any detectable counterparts in SuperCOSMOS Sky Survey or SDSS images), or detections due to cosmic rays, satellite trails, CCD defects, etc.

If an object was found to be incorrectly deblended or if the object’s parameters were obviously wrong, the object was re-extracted by manually changing the SEXTRACTOR extraction parameters until a satisfactory result was achieved. In addition, all low-quality regions in the survey (e.g. near CCD edges or defects) were carefully masked out, resulting in an effective survey area of 30.88 deg^2 .

2.2 Spectroscopy

To obtain spectroscopy for the MGC ($B_{\text{MGC}} < 20$ mag) we first turned to publicly available data and matched the MGC to the SDSS Data Release 1 (SDSS-DR1; Abazajian et al. 2003), 2dFGRS, 2QZ (Croom et al. 2004) and other smaller surveys. We then conducted our own redshift survey (MGCz), mainly using the Two Degree Field (2dF) facility on the Anglo-Australian Telescope (see Driver et al. 2005 for details). While the primary goal of this campaign was to obtain redshifts for those MGC galaxies without public data, we also targeted two other samples:

2.2.1 The all-object sub-region

The first of these additional samples consisted of *all* objects, irrespective of morphology, image classification or colour, in a small sub-region of the MGC. This all-object sub-region is defined as that part of the MGC strip which is bounded by $11^{\text{h}}49^{\text{m}}52^{\text{s}}.44 < \alpha < 12^{\text{h}}00^{\text{m}}08^{\text{s}}.45$ (J2000), i.e. MGC fields 56–61 (with only partial coverage of the end fields). The seeing in these fields ranged from 1.05 to 1.25 arcsec with the median at 1.15 arcsec, slightly better than the survey median of 1.27 arcsec. The effective area of this

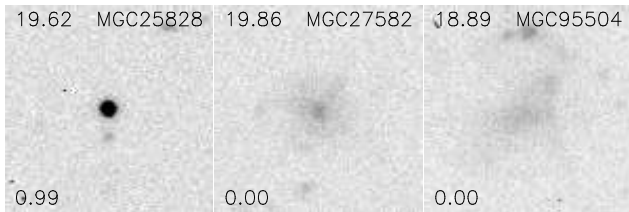


Figure 1. MGC postage stamps of the three objects in the all-object region without a good quality ($Q_z \geq 3$) spectrum. The labels give the object ID (upper right), B_{MGC} (upper left) and stellaricity (lower left) for each object. The image sizes are 33×33 arcsec².

region, after subtraction of the exclusion regions, is 1.1371 deg^2 and it contains 1552 objects (and 10 asteroids) in the range $16 \leq B_{\text{MGC}} < 20$ mag. The bright limit is set by the magnitude where stars begin to flood and the faint limit is that of the main MGCz galaxy survey.

We have at least one spectrum for each object in this sample and we give details of the spectroscopic identifications in Table 1. However, for three objects the quality of the data is too low to allow an identification or redshift measurement ($Q_z = 2$, see Driver et al. 2005). Hence the overall spectroscopic completeness is 99.8 per cent. The three objects without good quality spectra are shown in Fig. 1. For two of these (MGC27582 and MGC95504) there is no possibility of misclassification: they are clearly low SB galaxies and we will treat them as confirmed galaxies in the rest of the paper.

In contrast, the third object, MGC25828 (J115340.51 +001407.9), is unresolved (stellaricity = 0.99) and hence could be a misclassified galaxy. Since the number of such objects is small (cf. Table 1) even a single additional case would make a significant difference to our incompleteness estimates. Hence we take a closer look at this object in the following.

We have three independent 2dF spectra for MGC25828, one of which was contributed by the 2QZ (who could not identify it either), and these are shown in Fig. 2. Even though a high signal-to-noise continuum is common to all three spectra ($S/N \approx 12$) we were nevertheless unable to confidently identify this object because of the lack of emission and absorption features. A broad ‘bump’ near 4040 \AA is only evident in the bottom two spectra while the top spectrum shows two broad bumps at 5025 and 6185 \AA . If this variation is real, i.e. due to object variability and not some instrumental effect, then the object must vary on the timescale of one day (time difference between the top two spectra), while the similarity between the bottom two spectra (which were taken three years apart) must then be coincidental.

A strong optical continuum with no or only weak broad emission lines, and variability on the timescale of days are characteristics of blazars (e.g. Wagner & Witzel 1995). Indeed, if we interpret the broad bumps above as weak emission lines then they could possibly be identified as Ly α , C IV and C III] at $z \approx 2.24$ (cf. Fig. 2).

The possible identification of MGC25828 as a blazar is further supported by two facts: (i) The object has AGN-like colours as evidenced by its selection as a target by both the 2QZ and the SDSS QSO survey (who have not yet observed it). (ii) According to the SuperCOSMOS Sky Survey (Hambly et al. 2001) and USNO-B (Monet et al. 2003) catalogues this object has no significant proper motion. Hence it is not surprising that MGC25828 satisfies the Londish et al. (2002) selection criteria for BL Lac candidates in the 2QZ (even though it is missing from their published list of candidates; Londish, priv. comm.).

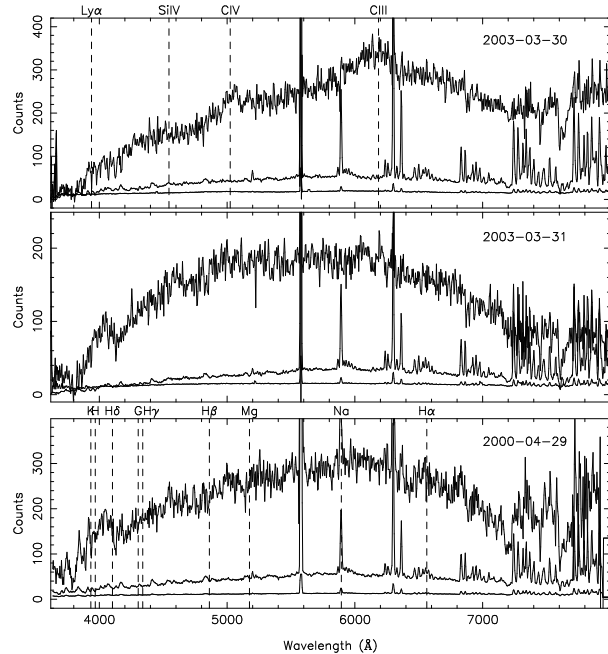


Figure 2. Three independent 2dF spectra of the possible blazar MGC25828. The top two spectra are from MGCz, while the bottom spectrum was obtained by the 2QZ. None of them are flux-calibrated. Each panel shows the object, mean sky and error spectra. The purpose of the sky spectra is to indicate the positions of strong sky lines and they have been scaled arbitrarily. The UT date of observation is also shown in each panel. The vertical dashed lines indicate the positions of prominent broad QSO emission lines at $z = 2.24$ (top panel) and stellar absorption features at $z = 0$ (bottom panel).

Table 1. Spectroscopic identifications of the complete sample of objects in the all-object region ($16 \leq B_{\text{MGC}} < 20$ mag).

Description	Number
Galaxies	444
MCs ^a	3
Stars	1083
QSOs	21
Unidentified (blazar or WD)	1
Total	1552

^aSpectroscopically identified galaxies which had been morphologically misclassified as stars.

On the other hand we do not observe any broad-band photometric variability. Comparing the object’s brightness in the SDSS and MGC images, which were taken one year apart, we find a difference of only 0.07 mag (see Cross et al. 2004 for the filter conversion). Also, the object does not appear to be a strong radio or X-ray source since it is not listed in either the FIRST or ROSAT All-Sky Survey (RASS) catalogues.

The lack of stellar absorption features in the spectrum of MGC25828 (cf. bottom panel of Fig. 2) means that this object could also be a DC white dwarf (e.g. Wesemael et al. 1993). However, it also implies that the observed continuum is unlikely to be due to a stellar population and so we can discard the possibility that this

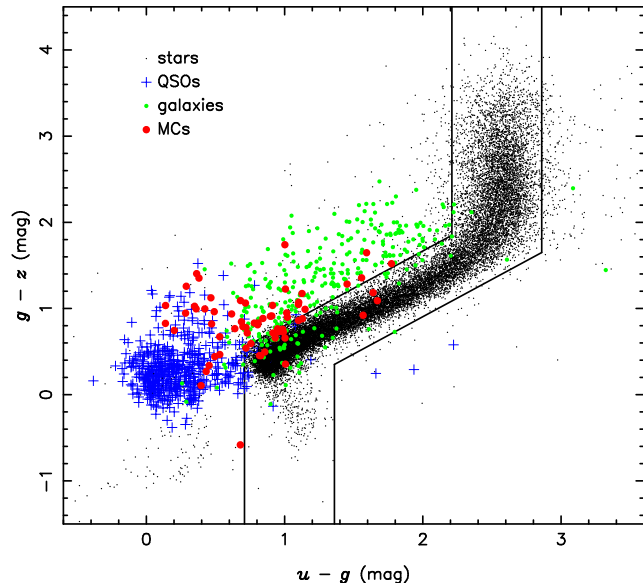


Figure 3. Colour–colour plot using SDSS-DR1 PSF magnitudes showing our colour selection of targets for additional observations of morphologically stellar objects outside of the all-object region. Black points and blue crosses show MGC stars and QSOs with $18 \leq B_{\text{MGC}} < 20$ mag respectively. We define the band between the solid lines as the ‘stellar locus’ in this colour–colour space. Green dots show a random sample of 300 galaxies in the same magnitude range. Note that PSF magnitudes are physically not very meaningful for extended objects; we only wish to indicate the degree of separation between stars and galaxies in this space. Red dots show all 65 spectroscopically identified galaxies in the MGC which had been morphologically misclassified as stars (MCs).

object is a galaxy. We are therefore reasonably certain to have identified *all* galaxies in the all-object region (within our magnitude limits).

2.2.2 Additional spectroscopy of stellar objects

Apart from the main galaxy survey and the all-object region, we also observed a third sample of targets when 2dF fibres were available. The target list for this sample comprised: (i) all morphologically stellar objects with $18 \leq B_{\text{MGC}} < 20$ mag that lie away from the stellar locus in $(u-g)-(g-z)$ colour–colour space, where the ‘stellar locus’ is defined in Fig. 3; (ii) a random subset of stellar objects that lie in the stellar locus ($18 \leq B_{\text{MGC}} < 20$ mag); (iii) stellar objects morphologically classified as galaxies by the SDSS-DR1 ($16 \leq B_{\text{MGC}} < 20$ mag). Objects were only targeted if they had not been observed previously by other surveys. Merging the incomplete observations of this target list with publicly available data yields 3223 secure identifications of morphologically stellar objects outside of the all-object region, 65 per cent of which were supplied by MGCz. Details are given in Table 2. The relatively high discovery rate of misclassified galaxies compared to the previous Section is presumably due to the colour selection. However, this sample is in no way complete. Since more than one survey has significantly contributed to this sample and since the magnitude limits, colour selection techniques and incompleteness levels of these surveys are different, it is very difficult to reliably construct its selection function. For example, we expect the spectroscopic completeness to the left of the stellar band in Fig. 3 to be very different from that within the band because of the MGCz colour selection.

Table 2. Additional spectroscopic identifications of morphologically stellar objects outside of the all-object region ($16 \leq B_{\text{MGC}} < 20$ mag).

Description	Number
MCs ^a	62
Stars	2625
QSOs	536
Total	3223

^aAs in Table 1.

However, even the space to the left will not be sampled homogeneously because of the colour selection of the 2QZ and SDSS QSO surveys. Simply ignoring these additional data does not help either because we specifically excluded objects already observed by these surveys from MGCz observations.

In Section 4.3 we will ignore these complications and apply a rudimentary incompleteness correction to this sample based on the selection function of the MGCz observations. In any case, at the very least this sample provides an indication of the properties of misclassified compact galaxies as well as a lower limit on their incidence.

3 PROPERTIES OF MISCLASSIFIED COMPACT GALAXIES

In total we have spectroscopically identified 65 compact galaxies (cf. Tables 1 and 2) that had been morphologically misclassified as stars from the imaging data (using the procedure described in Section 2.1). In the following we will refer to these objects as misclassified compact galaxies (MCs). We illustrate their morphological similarity to stars in Fig. 4, where we show a selection of their MGC images alongside the images of two stars. In Fig. 5 we compare their stellaricity values to the stellaricity distributions of stellar objects and non-misclassified galaxies.

In this Section we will investigate the properties of these 65 MCs in order to understand what types of galaxies are being missed due to misclassification. However, since these 65 MCs make up only about one half of the total number of MCs expected in the MGC (see Section 4) it is in principle possible that their properties are not fully representative of all MCs in general. Nevertheless, they provide a good indication of the types of objects that may be missed.

3.1 Spectral properties

Only five of the 65 MCs are absorption line galaxies and we show three example spectra in Fig. 6(a)–(c). Three of the absorption line MCs (MGC10809, MGC17413 and MGC34647) appear to be E+A galaxies (Dressler & Gunn 1983) since they have strong Balmer absorption with an $H\delta$ rest equivalent width (EW) of $> 5 \text{ \AA}$ superimposed on an elliptical galaxy spectrum. Although MGC10809 possibly has a weak $[O\text{II}] \lambda 3727$ emission line (cf. Fig. 6b), its EW is $< 2.5 \text{ \AA}$ and hence all three objects satisfy commonly used criteria to define E+A galaxies (e.g. Goto 2005).

Note also the unusual spectrum of MGC26040 (Fig. 6c). It has a very weak 4000 \AA break ($D_{4000} = 1.28$) and a blue, AGN-like $(u-g)$ colour (cf. Section 3.2). It is also a radio and X-ray source,

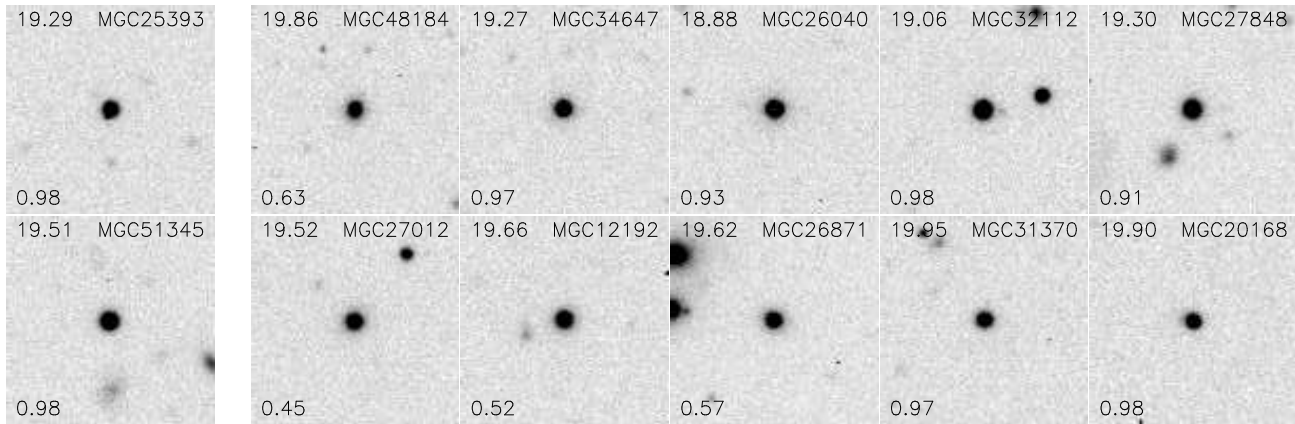


Figure 4. Right: MGC postage stamps of a sample of ten misclassified compact galaxies (MCs). Left: Images of two stars for comparison. Labels and image sizes are as in Fig. 1.

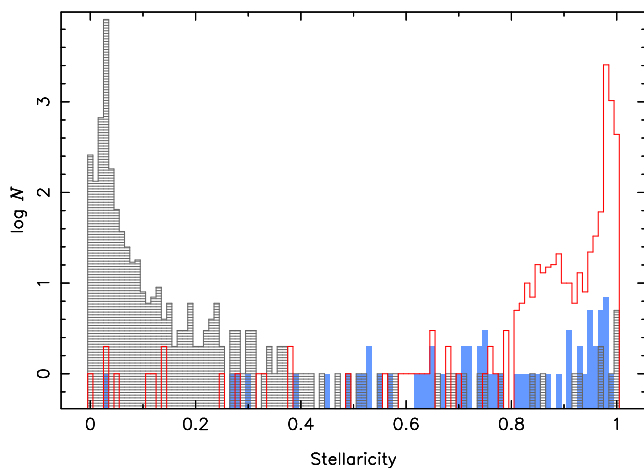


Figure 5. Stellaricity distributions of spectroscopically confirmed stars and QSOs (open red histogram), galaxies (hashed) and misclassified compact galaxies (MCs, solid blue).

with detections in FIRST, NVSS and RASS. Based on these properties Schwobe et al. (2000) and Anderson et al. (2003) independently classified MGC26040 as a probable BL Lac. This object also erroneously appears in the SDSS QSO catalogue of Schneider et al. (2003). Erroneously because Schneider et al. required a spectrum to show at least one broad emission line for the object to be included in the catalogue, and stressed that BL Lac objects were not included. Indeed, the object has been excised from the most recent version of the SDSS QSO catalogue (Schneider et al. 2005).

The spectra of 60 of our 65 MCs show nebular emission lines. The EUV photons that ionize the emitting gas may be provided by either hot massive stars from recent or ongoing star formation or by the non-thermal continuum of an active galactic nucleus (AGN) or both. In principle, the emission line spectrum is quite sensitive to the hardness of the ionizing radiation and hence emission line ratio diagrams are frequently used to distinguish between star-forming or H II region-like galaxies and narrow-lined (i.e. type 2) AGN, such as Seyfert 2 galaxies and low-ionization nuclear emission regions (LINERs). These line ratio diagnostics were pioneered by Baldwin, Phillips & Terlevich (1981) and further refined by Veilleux & Osterbrock (1987).

To construct an $[\text{O III}]/\text{H}\beta$ versus $[\text{N II}]/\text{H}\alpha$ line ratio diagram

we have measured the line fluxes of the 60 emission line MCs by first subtracting a locally fitted continuum and then fitting one or more gaussians as required. The $\text{H}\alpha$ - $[\text{N II}]$ complex was fitted with at least three components where the $[\text{N II}] \lambda\lambda 6548, 6584$ doublet was constrained to have the same width and redshift and a flux ratio of 1:3. For two galaxies we were able to improve the fit by adding a weak broad component in $\text{H}\alpha$ and $\text{H}\beta$ while five galaxies required a weak broad component in $\text{H}\alpha$ only, indicative of Seyfert 1.8 and 1.9 galaxies respectively. Hence we classify these seven objects as AGN and collectively refer to them as type 1.x AGN. Two example spectra are shown in Fig. 6(d)–(e).

In Fig. 7 we show the resulting line ratios for 44 of the 60 emission line MCs. The other 16 MCs are excluded from this plot because either their spectra do not cover $\text{H}\alpha$ (11 cases) or at least one of the four lines could not be detected with reasonable S/N (4 cases). Finally, one object was excluded because both the $\text{H}\alpha$ and $[\text{O III}] \lambda 5007$ lines appeared to be saturated.

The dashed line in Fig. 7 is the empirical upper envelope of star-forming galaxies found by Kauffmann et al. (2003a) and the solid line shows the theoretical upper limit for the location of pure starbursting galaxies in this diagram derived by Kewley et al. (2001). A number of galaxies lie between these lines and it is clear that it is not possible to perfectly separate star-forming galaxies from type 2 AGN. The reason is of course that nuclear activity and star-formation are not mutually exclusive phenomena and an object's emission lines may contain contributions from both. It is well known that star-formation may affect the line ratios not only of the lower luminosity LINERs (e.g. Ho et al. 1993) but also of the more powerful Seyfert 2s (e.g. Cid Fernandes et al. 2001).

Hence we follow Brinchmann et al. (2004) and divide our MCs into three groups: we label objects below the dashed line in Fig. 7 as star-forming galaxies (24 objects, green dots), those above the solid line as type 2 AGN (4 objects, red dots) and those in-between as composites (9 objects, orange dots). In Fig. 6(f)–(k) we show example type 2, composite and star-forming spectra.

We caution the reader that the above terminology is somewhat misleading because it suggests that all star-formation/AGN overlap is limited to the composite objects. That is not the case: we plot in Fig. 7 as red triangles the narrow components of the seven galaxies already identified as AGN by the presence of broad components. One of these objects lies below the Kauffmann et al. line, demonstrating that even objects labelled as 'star-forming' above may in fact contain an AGN (see also Simpson 2005). Similarly,

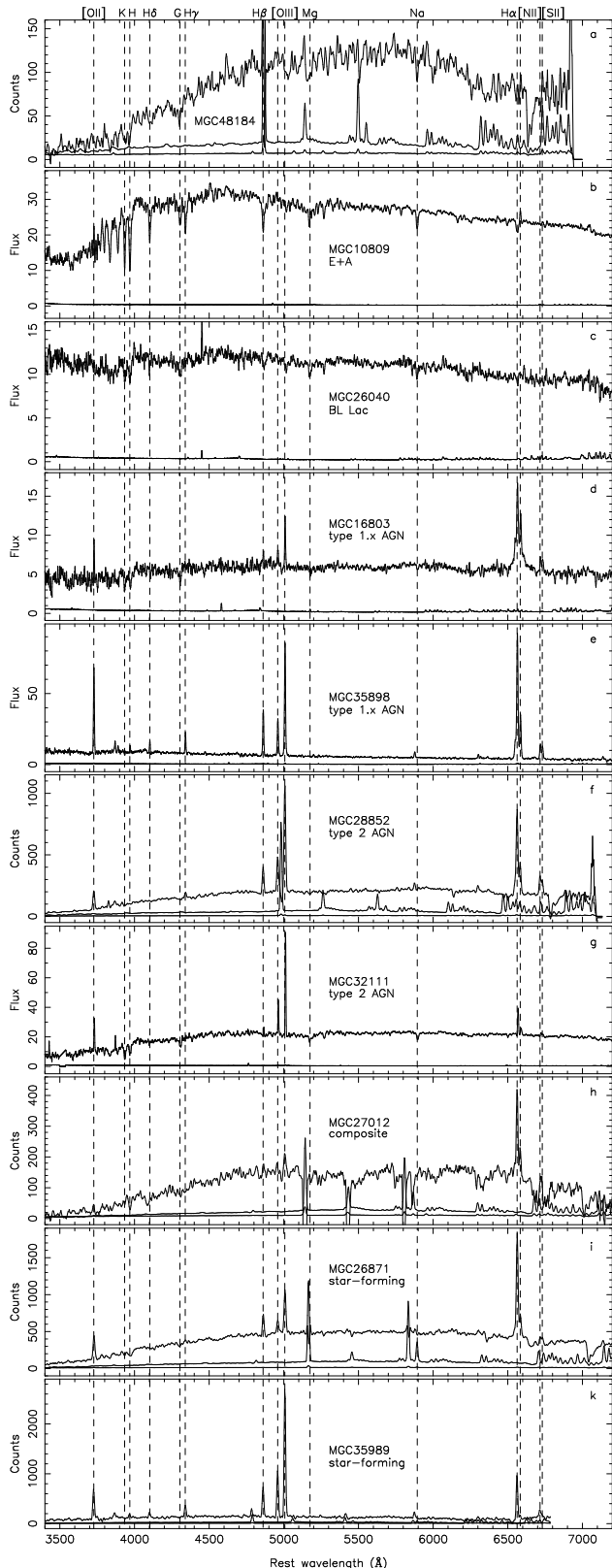


Figure 6. Rest-frame spectra of ten MCs representative of the various spectral classifications. We show the object, error and mean sky spectra (where available) which have been scaled arbitrarily. Only SDSS spectra are flux calibrated. The vertical dashed lines mark the locations of common nebular emission and stellar absorption features. (a) Absorption line galaxy. (b) Example E+A galaxy. (c) BL Lac. (d)–(e) Example MCs requiring a broad emission line component at least in $H\alpha$. (f)–(k) Example MCs classified as type 2 AGN, composite or star-forming galaxies on the basis of Fig. 7.

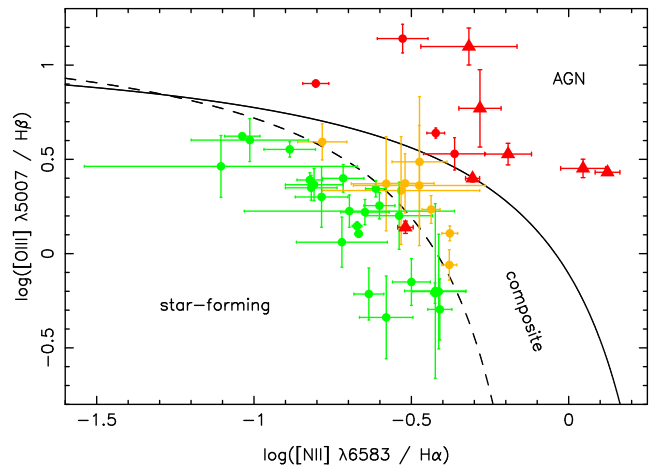


Figure 7. Emission line ratio diagnostic diagram used to classify emission line MCs. The dashed line shows the observed upper boundary of star-forming galaxies (Kauffmann et al. 2003a) while the solid line gives the theoretical upper limit for starbursts (Kewley et al. 2001). Accordingly, green dots mark star-forming galaxies, red dots denote type 2 AGN and orange dots show composites. Red triangles show the type 1.x AGN, using only their narrow line components.

a significant fraction of bona fide Seyfert 2s are known to contain a young stellar population (e.g. Storch-Bergmann et al. 2000) and Brinchmann et al. (2004) estimated that nearly 5 per cent of the total star formation rate density at $z \sim 0.1$ occurs in the host galaxies of type 2 AGN.

In addition, two further caveats apply to our classifications based on our emission line measurements: (i) Our 2dF spectra (from 2dFGRS and MGCz) are not flux calibrated. However, since the members of each line pair are quite close in wavelength we do not expect the flux calibration to have a large impact on the line ratios. (ii) We do not account for the underlying stellar Balmer absorption. Neglecting this absorption pushes galaxies in Fig. 7 toward the AGN regime. To assess the severity of this problem we compare our line ratio measurements to those of Tremonti et al. (2004) who carefully modelled and subtracted the stellar continuum (including the Balmer absorption) before emission line fitting. Eight of our objects in Fig. 7 were also in Tremonti et al.’s sample, but six of the 16 line ratio measurements cannot be compared to ours because of our use of a broad component. For the rest we find that Tremonti et al.’s ratios are smaller than ours by less than 0.05 dex in five cases, by 0.07 dex in one case, and by ~ 0.2 dex in four cases. From Fig. 7 we can see that a shift of the latter magnitude would change the classification of three of the type 2 objects and of most of the composites.

Of the 11 MCs whose spectra do not cover $H\alpha$ we find that six show evidence of a broad component in $H\beta$ and we add these six objects to the type 1.x AGN class. One further object (MGC21061) has an $[O\text{ III}]/H\beta$ ratio of 1.4, placing it firmly in the AGN regime of Fig. 7 irrespective of its unknown $[N\text{ II}]/H\alpha$ ratio. In fact this object shows broad $Mg\text{ II}$ emission and so we also classify it as a type 1.x AGN.

This leaves a total of nine emission line objects which we are unable to classify because at least one pair of emission lines is unavailable for various reasons. However, two of these objects appear to be almost exact superpositions of a small, faint galaxy and a foreground star, since they both show clear evidence of stellar absorption lines at $z = 0$ in addition to redshifted emission lines.

Table 3. Properties of all known 65 MCs in the MGC.

ID	z	$M_{B_{MGC}}^a$	R_e^b	$(u-g)_0^c$	$(g-z)_0^c$	$\log \frac{[O III]}{H\beta}$	$\log \frac{[N II]}{H\alpha}^d$	Class ^e	Comments ^f
Absorption line objects:									
MGC48184 J133616.13+000726.3	0.1461	−19.04	1.24	1.81	1.27				
MGC10809 J104329.26+001205.1	0.1326	−20.18	1.07	1.72	0.95			E+A	DR1: gal
MGC17413 J111146.63+000017.9	0.1104	−19.34	0.99	1.66	1.05			E+A	DR1: gal
MGC34647 J123243.45−000453.8	0.1875	−19.98	0.75	1.77	0.70			E+A	
MGC26040 J115404.55−001009.8	0.2535	−20.76	1.05	0.35	1.03			BL Lac	Sw, A: BL Lac; RASS; FIRST; DR1: gal; in all-object region
Emission line objects:									
MGC00704 J100140.13−000123.2	0.3497	−20.72	1.93	0.49	0.96	0.53	−0.19	t1.x AGN	bc H α ; S; DR1: gal
MGC03855 J101326.04−000136.4	0.2555	−20.13	1.84	1.00	1.74	1.18	—	t1.x AGN	bc H β ; RASS; FIRST
MGC16803 J111011.90+000352.7	0.2177	−19.37	1.63	0.29	1.26	0.77	−0.28	t1.x AGN	bc H α ; A: broad-line AGN; RASS; DR1: QSO
MGC20403 J112525.59−000301.5	0.3596	−20.83	1.87	0.28	0.95	0.67	—	t1.x AGN	bc H β
MGC21061 J112753.52+000518.0	0.4596	−21.75	2.96	0.36	1.00	1.36	—	t1.x AGN	bc Mg II; S; FIRST; DR1: gal
MGC29999 J121040.15−000315.5	0.3016	−20.17	2.63	0.36	1.40	—	—	t1.x AGN?	bad sky near H β ; bc H β ?
MGC32112 J122102.95−000733.3	0.3662	−21.46	1.55	0.62	0.94	0.14	−0.52	t1.x AGN	bc H α , H β ; S; A, W: NLSy1; RASS; FIRST; DR1: gal; 2QZ: NELG
MGC33386 J122804.66−000506.7	0.3190	−20.78	—	0.14	0.83	0.36	—	t1.x AGN	bc H β ; 2QZ: QSO
MGC35898 J123840.24−000744.0	0.2046	−19.64	1.87	0.45	0.34	0.43	0.12	t1.x AGN	bc H α ; K: LINER; FIRST; DR1: gal
MGC41402 J130611.20−000932.7	0.3925	−20.92	2.40	0.38	1.35	0.45	0.05	t1.x AGN	bc H α , Mg II; S; DV: variable; DR1: QSO
MGC55396 J140434.62−000800.1	0.3034	−20.30	2.55	0.42	0.99	0.40	−0.31	t1.x AGN	bc H α ; K: LINER; DR1: gal; 2QZ: NELG
MGC57877 J141207.92+000325.3	0.2344	−20.05	1.39	0.47	0.82	1.04	—	t1.x AGN	bc H β
MGC61874 J142631.76−000249.8	0.2928	−20.19	2.22	0.14	1.04	—	—	t1.x AGN	bad sky near [O III]; bc H β ; 2QZ: NELG
MGC67450 J144413.26+001118.4	0.2067	−20.11	2.45	0.47	1.12	1.10	−0.32	t1.x AGN	bc H α , H β
MGC27848 J120118.84−000654.6	0.1818	−19.86	1.36	1.03	0.61	0.53	−0.36	t2 AGN	
MGC28852 J120450.47−001159.5	0.1196	−18.46	0.92	0.74	0.72	0.64	−0.42	t2 AGN	
MGC32111 J122217.54−000744.1	0.1714	−20.26	2.50	1.79	1.16	1.14	−0.53	t2 AGN	Ka; FIRST; DR1: gal
MGC63901 J143053.30−000917.5	0.1231	−19.89	1.77	0.87	0.64	0.90	−0.80	t2 AGN	FIRST
MGC02455 J100702.72−000937.2	0.0666	−17.34	0.93	1.07	0.90	0.59	−0.78	C	
MGC20976 J112754.40−001341.7	0.0491	−16.28	0.42	1.03	0.71	0.33	−0.53	C	
MGC21348 J113005.55−001001.7	0.0684	−17.07	0.68	0.93	0.88	0.37	−0.58	C	
MGC22397 J113626.84+000456.7	0.1338	−18.66	0.86	0.90	0.52	−0.06	−0.38	C	2QZ: NELG
MGC27012 J115741.37−001332.7	0.0851	−17.76	0.84	1.16	0.87	0.49	−0.47	C	in all-object region
MGC34229 J123121.18−000647.2	0.0793	−17.10	0.73	1.14	0.65	0.36	−0.47	C	
MGC54685 J140108.42−000030.4	0.1117	−18.13	0.93	1.06	0.76	0.23	−0.44	C	
MGC56265 J140726.91+001154.1	0.1756	−19.92	1.60	1.20	0.74	0.11	−0.38	C	
MGC96267 J111523.85+000622.5	0.0277	−14.65	0.46	0.64	0.81	0.37	−0.52	C	
MGC04637 J101532.73−001337.6	0.0943	−18.10	1.40	1.30	1.03	−0.34	−0.58	SF	
MGC12192 J104947.47+001423.1	0.1215	−18.56	0.99	1.21	0.93	−0.20	−0.41	SF	
MGC14297 J105917.28+001232.8	0.1993	−20.24	2.32	1.22	0.63	−0.15	−0.50	SF	
MGC15183 J110403.13+000644.0	0.0760	−17.74	0.89	0.80	0.51	0.40	−0.72	SF	
MGC16641 J111014.20−000022.9	0.0919	−17.89	0.81	0.63	0.50	0.11	−0.67	SF	DR1: gal
MGC22174 J113423.54−001444.1	0.0770	−17.28	0.61	0.82	0.78	0.39	−0.82	SF	
MGC23590 J114130.16−000433.5	0.1107	−17.90	1.27	0.82	0.56	0.22	−0.65	SF	
MGC26871 J115821.52−000520.6	0.0799	−17.51	0.77	1.06	0.77	0.34	−0.61	SF	RASS; in all-object region
MGC27394 J120013.37−000747.7	0.0614	−16.56	0.35	0.86	0.50	0.60	−1.01	SF	
MGC27446 J120016.76−001119.0	0.0807	−17.81	0.92	1.05	0.75	0.20	−0.54	SF	

Table 3 – *continued*

ID	z	$M_{B_{\text{MGC}}}^a$	R_e^b	$(u - g)_0^c$	$(g - z)_0^c$	$\log \frac{[\text{O III}]}{\text{H}\beta}$	$\log \frac{[\text{N II}]^d}{\text{H}\alpha}$	Class ^e	Comments ^f
MGC27813 J120141.90–000502.8	0.0829	−17.69	0.51	1.07	0.71	−0.20	−0.42	SF	
MGC31360 J121830.69–001117.2	0.0849	−18.07	0.68	0.89	0.58	0.15	−0.67	SF	DR1: gal
MGC31370 J121754.42–001147.8	0.0708	−16.87	0.44	0.76	0.83	−0.30	−0.41	SF	
MGC33857 J123007.02–001123.4	0.0905	−17.62	0.64	1.19	1.03	−0.21	−0.64	SF	
MGC35989 J124032.96–001402.7	0.1646	−19.25	1.35	0.54	0.04	0.62	−1.04	SF	2QZ: NELG
MGC47144 J133229.12+001425.2	0.0804	−17.18	0.40	0.94	0.55	0.23	−0.70	SF	
MGC52270 J135230.99+000345.7	0.0833	−17.55	0.67	1.00	0.69	0.30	−0.79	SF	2QZ: NELG
MGC57241 J140846.88–001243.5	0.0950	−17.73	0.91	0.91	0.49	0.46	−1.11	SF	
MGC60772 J142229.09–000812.6	0.0543	−16.21	0.45	0.84	0.75	0.35	−0.82	SF	
MGC64370 J143243.74–000105.8	0.1303	−18.48	0.88	0.77	0.35	0.37	−0.81	SF	
MGC65997 J143754.03–001527.0	0.1400	−18.51	1.24	0.78	0.52	0.06	−0.72	SF	
MGC67179 J144048.09–000858.1	0.1212	−18.61	1.01	0.57	0.21	0.55	−0.89	SF	
MGC95276 J105526.00–000501.8	0.1081	−19.03	1.57	1.14	1.09	0.25	−0.60	SF	
MGC96202 J101416.19+001133.4	0.0713	−18.40	0.87	1.20	0.92	−0.21	−0.42	SF	
MGC00145 J095931.46–000013.3	0.2152	−19.64	1.33	1.01	0.59	0.16	—		
MGC34325 J123100.44+000402.0	0.4633	−21.14	2.61	0.85	0.20	0.36	—	t1.x AGN?	2QZ: NELG
MGC11178 J104353.73–001419.0	0.1005	−18.41	1.65	1.24	0.91				weak emission lines
MGC14790 J110156.38–000001.8	0.0733	−17.03	0.53	1.50	1.20				weak emission lines
MGC17184 J111122.09–000636.9	0.1231	−18.36	1.12	1.26	0.82		−0.46		weak emission lines
MGC35480 J123642.47–000946.6	0.0722	−16.97	0.43	0.72	−0.50				H α , [O III] saturated; 2QZ: NELG
MGC52589 J135243.21–000017.3	0.1589	−19.64	1.12	0.91	0.65	−0.14			H α in telluric line
MGC20168 J112428.81+000321.7	0.3283	−20.71	1.26	2.19	0.56	0.50	—	star+gal	
MGC28037 J120107.34–001639.4	0.2056	−20.50	1.23	1.25	0.14		—	star+gal	weak H β

^aAbsolute magnitude using $h_{100} = 1$, $\Omega_M = 0.3$, $\Omega_\Lambda = 0.7$. For the BL Lac and type 1.x objects we assume a power-law spectral shape and hence a K -correction of $K(z) = -(\alpha + 1) 2.5 \log(1 + z)$, where $\alpha = -0.5$. For all other objects we use the K -corrections of Driver et al. (2005, section 3.2).

^bPhysical half-light radius in units of h^{-1} kpc, where the observed apparent half-light radius, r_e , has been seeing-corrected using $r_0^2 = r_e^2 - 0.32 \Gamma^2$ (Driver et al. 2005, Appendix A), where Γ is the seeing FWHM. A ‘—’ indicates objects with $r_e < 0.6 \Gamma$.

^cRest-frame colours using SDSS-DR1 PSF magnitudes for the BL Lac and type 1.x objects, and model magnitudes for all others. K -corrections as above.

^dA ‘—’ indicates that the H α -[N II] complex is not covered.

^eSF = star-forming galaxy; C = star-forming/AGN composite; star+gal = superposition of a star and a galaxy.

^fbc = broad component; A = Anderson et al. (2003); DV = de Vries et al. (2003); K = Kniazev et al. (2004); Ka = Kauffmann et al. (2003a); S = Schneider et al. (2005); Sw = Schwoppe et al. (2000); W = Williams et al. (2002); RASS = ROSAT All-Sky Survey (Voges et al. 1999, 2000); FIRST = White et al. (1997).

We summarise our line ratio measurements and classifications in columns 7–9 of Table 3. Finally we note that several of the MCs classified as AGN have been previously classified by other authors or have been detected in X-ray or radio surveys (see the last column of Table 3). These findings broadly support our AGN identifications.

3.2 Colours

In Fig. 8 we compare the MCs to the general MGC galaxy and QSO populations in the rest-frame $(u-g)_0$ – $(g-z)_0$ colour–colour plane. In this comparison we use SDSS-DR1 PSF magnitudes for QSOs and for those MCs classified as type 1.x AGN or BL Lac, while we use model magnitudes for all other objects. For galaxies we also use the individual K -corrections derived by Driver et al. (2005). However, these will be inappropriate for those MCs whose broad-band fluxes are likely to be strongly contaminated by an AGN continuum (the type 1.x and BL Lac objects). For these objects and for QSOs in general we use a crude K -correction assuming a power-law spectral shape with index $\alpha = -0.5$ (Francis 1993). This correction does not account for the effects of broad emission lines which can contribute substantially to the flux in a given band. In fact, when considering colours this procedure is of course equivalent to applying no K -correction at all. The MCs’ rest-frame colours are listed in columns 5 and 6 of Table 3.

The galaxy distribution in Fig. 8 (small grey points) shows the well-known division between a red (\approx early-type) and a blue (\approx late-type) population (e.g. Baldry et al. 2004), while the QSOs (crosses) exhibit their characteristic UV excess. We note that low- z QSOs (red crosses) are somewhat redder in $(g-z)_0$ than the bulk of QSOs at higher redshifts (cyan crosses) due to $H\alpha$ falling in the z -band and, presumably, contamination from the host galaxies (see also Richards et al. 2001).

The redshift range of the low- z QSOs was chosen to coincide with that of the type 1.x AGN (i.e. $0.2 < z < 0.46$) and indeed we find that their colours are matched by the BL Lac (blue square) and by 12 out of 14 of our type 1.x AGN (red triangles). This indicates that the broad-band UV-visual fluxes of these MCs are indeed dominated by an AGN continuum and not by starlight, supporting our identification of these objects as AGN based on their emission lines.

One type 1.x (MGC35898) is somewhat bluer in $(g-z)_0$ than the rest, which is probably due to vigorous star-formation activity which is indicated by strong, narrow high order Balmer line emission (cf. Fig. 6e). In contrast, the 14th type 1.x (MGC03855) is significantly redder in both colours. However, it is both an X-ray and radio source and so its identification as an AGN is reasonably secure. This object may well be reddened by dust in the host galaxy (Richards et al. 2003).

In contrast to type 1.x objects, the AGN contribution to the continua of type 2 objects is extremely small (Kauffmann et al. 2003a), even in their nuclear regions (Schmitt, Storchi-Bergmann & Fernandes 1999), and hence their broad-band colours are expected to be dominated by their host galaxies. Indeed, the colours of our four type 2 objects (red dots) are quite different from those of the QSOs but are consistent with normal galaxies.

In a broad-brush sense the properties of the host galaxies of type 2 AGN are known to depend on the AGN’s [O III] $\lambda 5007$ luminosity (Kauffmann et al. 2003a). For example, the mean stellar ages (as measured by D_{4000} and the $H\delta$ EW) of the hosts of low-luminosity AGN are similar to those of normal early-type galax-

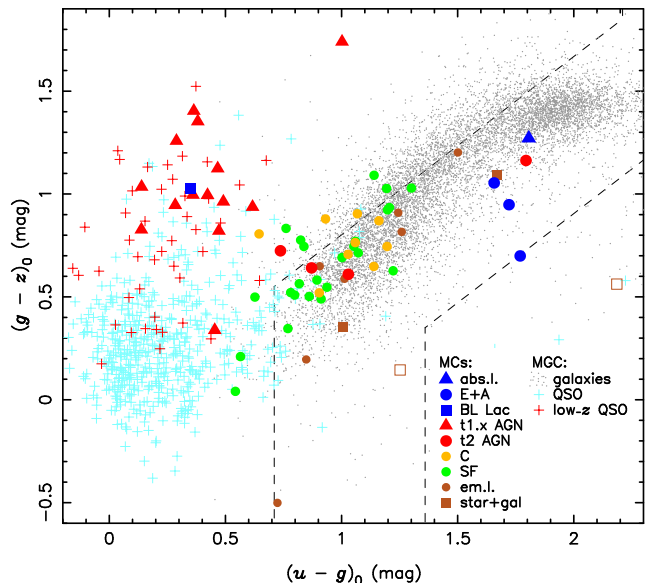


Figure 8. Rest-frame colour–colour plot of all 65 MCs and the general MGC galaxy and QSO populations as indicated. Abbreviations are those of Table 3. ‘abs.l.’ and ‘em.l.’ refer to absorption and emission line objects without further classification. ‘low- z QSOs’ refers to QSOs in the same redshift range as type 1.x AGN, i.e. $0.2 < z < 0.46$. Star/galaxy superpositions are shown with and without K -corrections (open and solid brown squares respectively). We use SDSS-DR1 PSF magnitudes for QSOs, type 1.x AGN and the BL Lac, and model magnitudes for all other objects. The dashed lines show the (observed-frame) ‘stellar locus’ defined in Fig. 3.

ies, while high-luminosity AGN reside in hosts with younger stellar populations, similar to those of normal late-type galaxies. This would explain why we observe both red and blue type 2 objects. To check whether our objects are consistent with the above trend we need to measure their [O III] luminosities. Unfortunately, only the red object’s spectrum (MGC32111) is flux calibrated: it turns out to be of intermediate luminosity ($L_{[\text{O III}]} = 10^{7.74} L_{\odot}$) which is however low enough for the D_{4000} and $H\delta$ EW distributions of type 2s (cf. fig. 12 of Kauffmann et al.) to still overlap comfortably with the ranges typical for normal early-type galaxies ($D_{4000} > 1.7$ and $H\delta$ EW $< 1 \text{ \AA}$). The strength of our object’s 4000 \AA break ($D_{4000} = 1.7$) does indeed fall in this overlap region and indicates the presence of an old stellar population, but its $H\delta$ EW ($= 1.9 \text{ \AA}$) is somewhat too high for normal early-types. In fact, MGC32111 is displaced from Kauffmann et al.’s (2003b) well-defined D_{4000} – $H\delta$ relation. This occurs frequently for type 2s and may be interpreted as a sign of a significant burst of star-formation in the past two Gyr (Kauffmann et al. 2003a).

An old, evolved stellar population together with a significant, truncated two-Gyr-old starburst has also been invoked by Balogh et al. (2005) to explain the $(r-K)$ and $(u-g)$ colours of E+A galaxies, and so it is perhaps not surprising that MGC32111 and our three E+As (blue dots) are found in a similar region of Fig. 8. In this scenario a galaxy in the red locus in Fig. 8 is moved down and to the left onto the blue sequence by a burst of star-formation. After the burst’s truncation the galaxy’s UV-blue colour reddens again quite rapidly while redder colours evolve much more slowly, leaving the galaxy below the red locus in Fig. 8. We note that our E+As’ $(u-g)$ colours are indeed identical to those found by Balogh et al. (2005).

The only MC that is a normal absorption line galaxy (blue

triangle, cf. Fig. 6a) lies among the general red galaxy population as expected.

The MCs identified as star-forming (green dots) or composite (orange dots) in the previous Section occupy the blue half of the general blue galaxy sequence. The star-forming MCs extend to its very blue tip. The three objects furthest along the sequence all show higher order Balmer lines (e.g. MGC35989, see Fig. 6k), indicative of strong star-formation activity.

Notice the odd locations in Fig. 8 of the two likely star/galaxy superpositions (open brown squares). These are not too surprising: if the broad-band fluxes of these objects are dominated by the stars rather than the galaxies then their K -corrections are meaningless. Indeed, the objects' observed-frame colours (solid brown squares) place them squarely in the centre of the stellar locus (dashed lines, cf. also Fig. 3).

The unclassified emission line objects (brown dots) mostly lie along the general blue sequence. The reddest three objects are also those with the weakest emission lines while the object near the tip of the blue sequence (MGC34325) again shows high order Balmer lines. However, we have re-plotted Fig. 8 using PSF magnitudes and QSO K -corrections for the unclassified objects to see whether any would lie among the low- z QSOs. This was indeed the case for MGC34325 and so this object could also be a type 1.x AGN. Finally, the object at $(g-z)_0 = -0.5$ is the one with saturated $H\alpha$ and $[O III] \lambda 5007$. It also shows very strong high order Balmer lines and may hence be undergoing an extreme starbursting phase.

3.3 Redshifts, luminosities and sizes

In Fig. 9 we show the distribution of the MCs in the absolute magnitude–redshift plane, along with the rest of the MGC galaxy population. To calculate the absolute magnitudes we use the same K -corrections as in the previous Section and we list the MCs' redshifts and magnitudes in columns 2 and 3 of Table 3.

The MCs appear to be segregated in the M_B - z plane according to their type: star-forming and composite objects mostly lie along the faint magnitude limit at low redshifts, while the type 1.x AGN all lie at $z > 0.2$ and correspondingly brighter magnitudes. In fact, the only other MCs at $z > 0.2$ are the BL Lac, the star/galaxy superpositions and two unidentified emission line objects. One of these lies at $z \approx 0.2$ and the other is MGC34325 (at $z = 0.46$) which was already suspected of being a type 1.x in the previous Section. Assuming that MGC34325 is indeed a type 1.x, we find that *all* MCs whose continua are *not* dominated by starlight lie at $z > 0.2$ and $M_B < -19.3$ mag, while the 'real' galaxies among the MCs all lie at $z < 0.22$ and $M_B > -20.3$ mag, so that there is almost no overlap between the two groups. In particular, this produces a pronounced bimodality in the MCs' magnitude distribution. From now on we will generically refer to these two groups as 'real' and 'AGN-dominated' MCs (47 and 18 objects respectively, where the latter group also contains the star/galaxy superpositions).

So why are 'real' and 'AGN-dominated' MCs distributed so differently? And why are both groups distributed differently from the general MGC galaxy population?

For the 'AGN-dominated' MCs two obvious explanations come to mind. (i) It is well-known that the frequency of nuclear activity decreases with decreasing redshift (e.g. Croom et al. 2004). This is also seen in the MGC where the density of QSOs falls off rapidly towards lower z . (ii) The frequency of nuclear activity might also decrease with luminosity or size. In this case the hosts of the low- z counterparts of our type 1.x would probably be resolved and so they would not be selected as MCs. To test this explana-

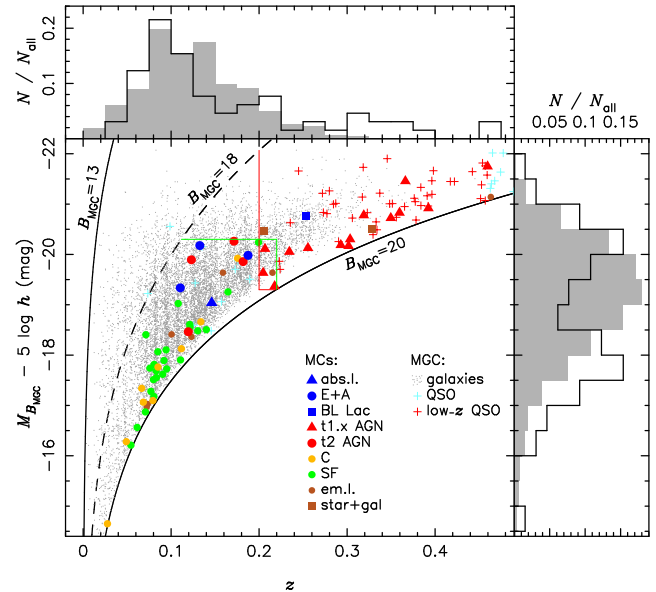


Figure 9. Absolute magnitude vs. redshift for all 65 MCs and the general MGC galaxy and QSO populations. Symbols are as in Fig. 8. The solid lines show the bright and faint apparent magnitude limits of the MGC (using the maximum and minimum K -correction respectively) while the dashed line marks the approximate bright magnitude limit of MCs ($= 18$ mag, cf. Section 2.2.2). The green and red lines show the limits of the regions occupied by the 'real' and 'AGN-dominated' MCs respectively. The side panels show the projected normalised distributions for the MCs (solid lines) and for the general MGC galaxy population (grey shaded histograms).

tion we would have to fit the emission lines of all resolved MGC galaxies. However, from Fig. 8 it is already clear that only very few resolved galaxies with QSO-like colours exist.

To understand the distribution of the 'real' MCs it is helpful to consider their magnitude and size selection limits simultaneously. In Fig. 10 we show the 'real' MCs along with the rest of the MGC in the physical size–absolute magnitude plane. To be able to compare the sizes with each other, especially in the case of small galaxies, we have applied the seeing correction of Driver et al. (2005). The MCs' sizes are listed in column 4 of Table 3.

First of all we notice the luminosity–size relation of galaxies: fainter galaxies tend to be smaller than brighter ones. This already explains why in Fig. 9 the 'real' MCs are mostly found near the faint magnitude limit: at a given redshift, the smallest galaxies are also the faintest. However, this should be true at all redshifts and so this relation by itself does not explain why 'real' MCs are preferentially found at lower z .

The polygon in Fig. 10 encloses the observable parameter space for galaxies at $z = 0.08$. It is determined by the MGC's apparent magnitude, size and low SB limits. These selection limits will be discussed further in Section 4 (see Fig. 11 and accompanying text). The minimum size limit, r_{\min} , is of particular interest here because MCs are expected to have apparent sizes $r_e \lesssim r_{\min}$. The three curved diagonal lines in Fig. 10 show how the top part of the polygon moves as a function of redshift. Essentially, they show the locations of galaxies with $r_e = r_{\min}$ and $B_{\text{MGC}} = 13, 18$ and 20 mag respectively (top left to bottom right). We shall refer to the last of these as the 'small faint line' (SFL). Evidently, galaxies below the SFL cannot possibly have sizes smaller than r_{\min} , no matter what their redshifts are.

The point of this plot is that the slope of the SFL is different

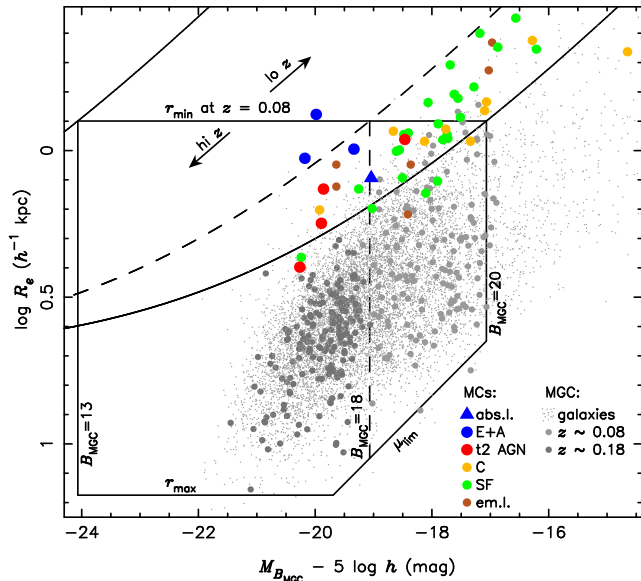


Figure 10. Seeing-corrected physical size vs. absolute magnitude for ‘real’ MCs and the general MGC galaxy population as indicated. The large, light and dark grey dots refer only to galaxies in the range $18 < B_{\text{MGC}} < 20$ mag. The polygon shows the various selection limits at $z = 0.08$: the MGC’s apparent magnitude limits, the minimum and maximum size limits as well as the low SB limit. The vertical dashed line shows the bright limit of the MCs as in Fig. 9. The diagonal lines show how the top part of the polygon moves as a function of z . The exact locations of the polygon and the lines depend on the assumed K -correction and seeing. Here we have used median values for both.

from the slope of the luminosity–size relation of the galaxies. The SFL actually curves away from the galaxy locus at brighter magnitudes and hence does not equally cut into the galaxy population at all luminosities. In fact, at the highest luminosities there is an almost empty region between the galaxy locus and the SFL and we must conclude that galaxies are very rare in this part of parameter space. To make this point clearer we highlight in Fig. 10 galaxies at $z \approx 0.08$ and $z \approx 0.18$ by large light and dark grey points respectively. For clarity we only show objects with $18 < B_{\text{MGC}} < 20$ mag. The low- z population reaches all the way to r_{min} and so it is not surprising to find galaxies smaller than r_{min} (and hence ‘real’ MCs) at $z \approx 0.08$. In contrast, the high- z population does not quite reach to the SFL and hence cannot reach to r_{min} , implying that galaxies do not exist beyond this limit either (unless the size distribution is bimodal).

Put simply, the distribution of the MCs in Figs. 9 and 10 is explained by the fact that the MGC’s minimum size limit only affects faint galaxies and that the MGC is already complete at high luminosities.

3.4 Implications

In the previous Sections we have seen that the spectra, colours, magnitudes and redshifts of 18 of our 65 MCs indicate that their broad-band fluxes are not dominated by starlight. In the context of deriving a luminosity function these objects must be considered a contamination. In addition, having found them among the MCs raises the possibility that the non-misclassified compact galaxies are similarly contaminated. If erroneously included in the analysis

these ‘AGN-dominated’ galaxies could significantly bias our LF estimates.

We have therefore subjected all non-MC galaxies with $r_e < r_{\text{min}} + 0.1$ arcsec to an analysis of their emission lines and colours along the lines of Sections 3.1 and 3.2. There are 192 such galaxies but we have found only two type 1.x objects among them. Hence the high fraction of ‘AGN-dominated’ objects among the MCs must be due to the colour selection of morphologically stellar targets. In any case, from now on we will exclude all 20 ‘AGN-dominated’ compact galaxies from all further analysis.

4 MGC INCOMPLETENESS AT HIGH SB

In order to quantify the MGC’s incompleteness due to the misclassification of compact galaxies as stars we will now restrict ourselves to the complete dataset from the 1.14 deg^2 all-object region described in Section 2.2.1. 446 of the 1552 objects in this region are confirmed galaxies (cf. Table 1). Of these, two objects are MCs, i.e. they had originally been misclassified as stars. (The third MC in this region is ‘AGN-dominated’ and will not be considered here.)

The goal of this Section is now to use the MCs in the all-object region to answer the following two questions: (i) How reliable is the MGC’s high SB selection limit (as determined by Driver et al. 2005), not just in the all-object region but for the survey as a whole? (ii) How many galaxies beyond this limit were missed by the MGC? In other words we wish to determine the MGC’s incompleteness due to misclassification as a function of SB (or size, see below). Since the number of misclassified galaxies must depend to some extent on seeing, this task is complicated, at least in principle, by the fact that the typical seeing of the all-object region is different from that of the MGC as a whole. Although the difference is only 10 per cent we have no way of knowing a priori whether it is important or not.

We begin by recalling that the MGC’s high SB limit is in fact a minimum size limit (see Appendix A of Driver et al. 2005). We use the half-light radius, r_e (in arcsec), as our size measure, which is defined as the semi-major axis of the ellipse containing half of the object’s total flux (as measured by SExtractor’s BEST magnitude). In Fig. 11(a) we show the distribution of objects from the all-object region in the r_e – B_{MGC} plane. The grey shaded areas show the various selection limits: the imposed bright and faint magnitude limits of 16 and 20 mag respectively (see Section 2.2.1), the limiting SB and the maximum and minimum size limits. We determined the latter three limits by simulating galaxies over the whole r_e – B_{MGC} plane using the image characteristics of the real MGC data, and extracting the objects in the same manner as the real data (see Appendix A of Driver et al. 2005). Here we are only concerned with the minimum size limit, r_{min} .

Driver et al. (2005) defined r_{min} as the minimum r_e at which a galaxy can still be *reliably* distinguished from stars. To derive r_{min} they reasoned as follows: the ability to distinguish a galaxy from stars depends primarily not on the absolute value of the galaxy’s r_e but rather on the distance of the galaxy to the stellar locus in r_e -space, where the scale of that distance is set by the width of the stellar r_e distribution. Obviously, the observed r_e values of stars and small galaxies are affected by seeing, and hence r_{min} must be a function of seeing. Driver et al. observed that for the MGC the median r_e value of stars is given by 0.6Γ , where Γ is the seeing FWHM, and that the width of the stellar r_e distribution is independent of seeing. These simple considerations imply $r_{\text{min}} = 0.6\Gamma + \Delta$, and using the simulations they determined

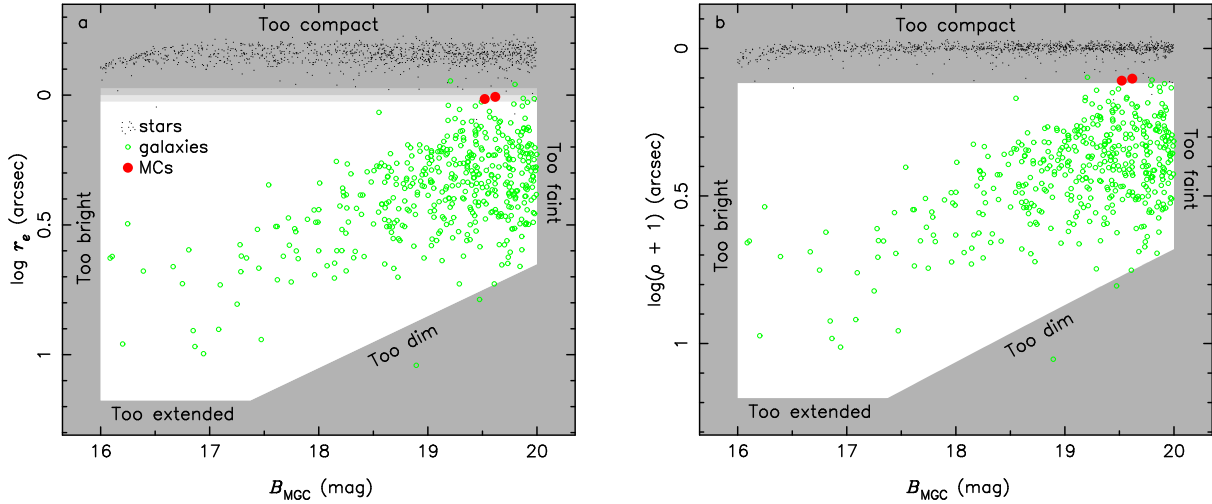


Figure 11. (a) Distribution of objects from the all-object region in the observed half-light radius–magnitude plane. Stars and QSOs are marked by small black points, galaxies by green open circles and misclassified compact galaxies by large solid red dots. Grey shaded areas show the observational selection limits discussed in the text. The seeing dependence of the minimum size limit is indicated by different levels of grey shading. We note in passing that the low SB and maximum size limits are *not* the absolute detection limits but rather the limits to which accurate photometry is possible. The slight increase of the stars’ r_e at the brightest magnitudes is due to the onset of flooding. (b) Same as (a) but replacing r_e with $\rho = r_e - 0.6 \Gamma$, i.e. the difference between an object’s r_e and the median r_e of stars observed in the same seeing.

$\Delta = 0.31$ arcsec. The seeing dependence of r_{\min} is represented in Fig. 11(a) by using different levels of grey shading for the best, median and worst seeing encountered in the all-object region.

The above also implies that $\rho = r_e - 0.6 \Gamma$ is a useful measure of an object’s similarity to stars. In Fig. 11(b) we plot the distribution of galaxies and stars in the ρ - B_{MGC} plane. The transformation $r_e \rightarrow \rho$ removes the seeing dependence of the stellar locus [cf. panel (a)], aligning all stars around $\rho = 0$ while preserving the width of the stellar r_e distribution. The minimum size limit is now simply given by $\rho_{\min} = 0.31$ arcsec and is also seeing independent. Note however that for a galaxy ρ is *not* seeing independent. While a galaxy moves downwards in Fig. 11(a) when observed under worse seeing conditions, it moves upwards in panel (b).

From Fig. 11(b) we can see that the two MCs lie near ρ_{\min} and other galaxies, which were correctly identified as such, exist at similar ρ values, indicating that the probability of misclassifying such galaxies is not 1. Both MCs lie beyond the minimum size limit, resulting in 100 per cent completeness within the selection limits, while the completeness at $\rho < \rho_{\min}$ is ~ 50 per cent (two out of the four galaxies in this range were misclassified).

We would now like to estimate the probability of misclassifying a galaxy and the resulting incompleteness for the full MGC more quantitatively. First, we define some notation. In the following N_g and N_{MC} denote the numbers of galaxies that were actually identified as such and of those that were misclassified as stars respectively. Hence the true number of galaxies is given by $N_G = N_{\text{MC}} + N_g$. The superscripts ‘AO’ and ‘MGC’ refer to objects in the all-object region and in the full survey region respectively.

Now consider the binomial probability, p_g , that a galaxy is morphologically misclassified as a star from the imaging data by the procedure described in Section 2.1. It follows from the discussion of the minimum size limit above that p_g should only be a function of ρ and that $p_g(\rho)$ is the same for any observation. The number of galaxies that are actually misclassified in a given observation is then determined by the distribution of galaxies in ρ , $n_G(\rho)$, which in turn depends on the seeing. We would like to estimate the

number of misclassified galaxies in the MGC with ρ larger than some ρ_{lim} :

$$N_{\text{MC}}^{\text{MGC}}(\rho_{\text{lim}}) = \int_{\rho_{\text{lim}}}^{\infty} n_{\text{MC}}^{\text{MGC}}(\rho) d\rho = \int_{\rho_{\text{lim}}}^{\infty} p_g(\rho) n_G^{\text{MGC}}(\rho) d\rho, \quad (1)$$

where we need to measure $p_g(\rho)$ from the all-object region. Ideally, we would estimate it as

$$p_g(\rho) = \frac{n_{\text{MC}}^{\text{AO}}(\rho)}{n_G^{\text{AO}}(\rho)} \quad (2)$$

in small bins of ρ . However, from Fig. 11(b) it is clear that the interesting region of ρ near ρ_{\min} is not populated densely enough to do this. We adopt two approaches to deal with this.

4.1 Parameterising $p_g(\rho)$

In the following we will assume a functional form for $p_g(\rho)$ and use the data to constrain the model’s parameter(s). Which functional form to use? Clearly, $p_g(\rho)$ should rise monotonically from 0 at $\rho \gg \rho_{\min}$ to 1 at $\rho \gtrsim 0$. Furthermore, given the paucity of data, the model should have at most two parameters. In general, these two parameters will characterise in some sense the ‘position’ and steepness of $p_g(\rho)$. Constructing a one-parameter model will require fixing one of these at some a priori value. The only choice that is not completely arbitrary seems to be $p_g(0) = 1$.

Using these general considerations as a guideline we now choose the following four models:

$$p_g^{\text{lin}}(\rho) = \begin{cases} 1 & \rho \leq 0 \\ 1 - c\rho & \text{for } 0 < \rho < \frac{1}{c} \\ 0 & \frac{1}{c} \leq \rho \end{cases} \quad (3)$$

$$p_g^{\text{gaus}}(\rho) = \begin{cases} 1 & \text{for } \rho \leq 0 \\ \exp\left(-\frac{\rho^2}{\sigma^2}\right) & \rho > 0 \end{cases} \quad (4)$$

$$p_g^{\text{cos}}(\rho) = \begin{cases} 1 & \rho \leq 0 \\ 0.5 [1 + \cos(\omega\rho)] & \text{for } 0 < \rho < \frac{\pi}{\omega} \\ 0 & \frac{\pi}{\omega} \leq \rho \end{cases} \quad (5)$$

$$p_g^{\text{erf}}(\rho) = 0.5 \left[1 - \text{erf} \left(\frac{\rho - \rho_{50}}{\beta} \right) \right]. \quad (6)$$

We have chosen three different one-parameter models in order to be able to test the sensitivity of the results to the precise functional form. In each case the free parameter (c , σ , ω) controls the steepness with which p_g declines to 0. In contrast we have chosen only one two-parameter model (the error function) because, as we shall see below, such models are already over-fitting the sparse data.

We now fit these models to the data from the all-object region using maximum likelihood. The likelihood function is given by

$$\mathcal{L} \propto \prod_{i=1}^{N_{\text{MC}}^{\text{AO}}} p_g(\rho_i) \prod_{j=1}^{N_g^{\text{AO}}} [1 - p_g(\rho_j)], \quad (7)$$

where the first product runs over all MCs and the second product over all other galaxies in the all-object region. Maximising this function with respect to the model parameters yields the results shown in panels (a)–(b) of Fig. 12, where the grey-shaded regions indicate 90 per cent confidence ranges.

Due to its additional free parameter the erf model behaves quite differently from the other models. It rises quite steeply just below ρ_{min} to accommodate the observed misclassified fraction of ~ 50 per cent in this region (cf. Fig. 11b) and predicts that essentially all galaxies with $\rho \lesssim 0.18$ arcsec should be misclassified. The other three models exhibit a more gentle rise, with the cosine and gaussian models resulting in very similar p_g curves. The smallness of the errors on p_g for small and large ρ values is of course a consequence of having assumed a specific functional form.

We now estimate the number of misclassified galaxies in the full MGC as

$$\begin{aligned} n_{\text{MC}}^{\text{MGC}}(\rho) &= p_g(\rho) n_{\text{g}}^{\text{MGC}}(\rho) \\ &= p_g(\rho) [n_{\text{MC}}^{\text{MGC}}(\rho) + n_{\text{g}}^{\text{MGC}}(\rho)] \\ &= \frac{p_g(\rho)}{1 - p_g(\rho)} n_{\text{g}}^{\text{MGC}}(\rho) \end{aligned} \quad (8)$$

and define the incompleteness of galaxies with $\rho > \rho_{\text{lim}}$ due to misclassification as

$$I_g(\rho_{\text{lim}}) = \frac{N_{\text{MC}}^{\text{MGC}}(\rho_{\text{lim}})}{N_{\text{MC}}^{\text{MGC}}(\rho_{\text{lim}}) + N_g^{\text{MGC}}(\rho_{\text{lim}})}. \quad (9)$$

$N_g^{\text{MGC}}(\rho_{\text{lim}})$ is shown in panel (c) of Fig. 12. Recall that according to the erf model essentially all galaxies with $\rho \lesssim 0.18$ arcsec should have been misclassified as stars. However, from Fig. 12(c) we can see that a few galaxies with $\rho < 0.18$ arcsec were in fact identified in the full survey. This causes the erf model to predict an infinite number of misclassified galaxies. This unrealistic result is of course due to the paucity of data in the all-object region compared to the number of free parameters of the erf model, which is also reflected by the large error on p_g^{erf} shown in in Fig. 12(b). We will not consider this model any further.

Note also that the few observed galaxies at small ρ values also justify our choice of $p_g(0) = 1$ for the one-parameter models. Moving the $p_g = 1$ point to a larger ρ value would have caused the same problem as above.

The incompleteness resulting from the linear, gaussian and cosine models is shown in panel (d) of Fig. 12. For a given model we can now read off the numbers that were the goal of this Section: (i) the incompleteness of galaxies within the selection limit, i.e. at $\rho_{\text{lim}} = \rho_{\text{min}}$ where the MGC was assumed to be complete by Driver et al. (2005) and (ii) the MGC’s overall incompleteness. We summarise these values in columns 2 and 4 of Table 4 respectively.

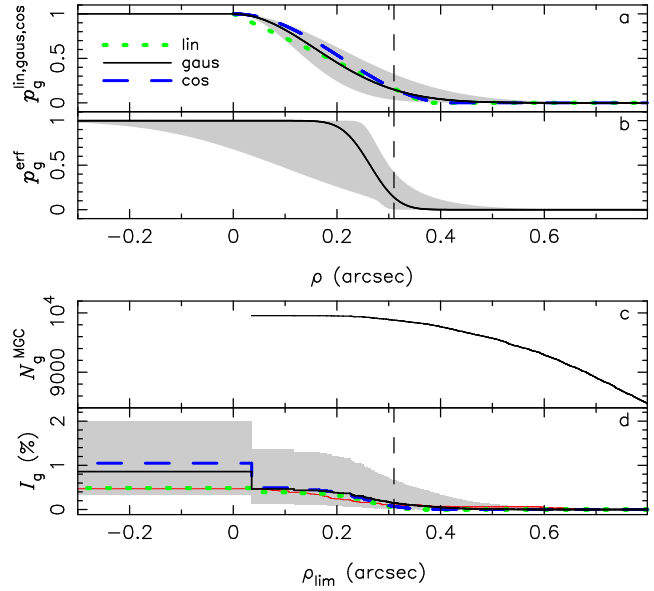


Figure 12. (a) Best fit models of the binomial probability of misclassifying a galaxy as a function of $\rho = r_e - 0.6\Gamma$, using the linear, gaussian and cosine models of equations (3)–(5) as indicated. The fits are obtained from the observed abundance of MCs in the all-object region, where we can be certain that *all* galaxies have been identified. The grey shaded area shows the 90 per cent confidence range for the gaussian model. (b) Same as (a) for the erf model of equation (6). (c) Number of observed galaxies (i.e. those that were originally identified as such) in the full MGC survey region with $\rho > \rho_{\text{lim}}$. (d) Estimates of the incompleteness of galaxies with $\rho > \rho_{\text{lim}}$ due to their misclassification as stars based on the binomial probabilities in panel (a) and the number of galaxies in panel (c). The thin red line is the incompleteness derived from all known (‘real’) MCs in the full MGC survey region. Since this sample is incomplete (cf. Section 2.2.2), this line is a strict lower limit to the true incompleteness. The grey shaded area shows the 90 per cent confidence range for the gaussian model and the vertical dashed line marks the minimum size limit for the reliable detection of galaxies adopted by Driver et al. (2005).

We also show in column 6 the incompleteness of galaxies beyond the selection limit.

From Fig. 12(d) we can see that the differences between the three models are smaller than the random errors (shown only for the gaussian model by the grey shaded area). Hence, given the size of the errors, the results do not depend sensitively on the precise shape of the assumed functional form of p_g .

Nevertheless, the incompleteness estimate provided by the linear model is somewhat lower than that of the other two models and may in fact be too low. In Fig. 12(d) we plot as a thin red line the incompleteness derived from *all known* ‘real’ MCs in the MGC (47 in total), i.e. those in the all-object region as well as those discovered through our additional spectroscopy of stellar objects described in Section 2.2.2. Since this sample is itself incomplete, the incompleteness derived from it must be considered a strict lower limit to the true incompleteness. The estimate from the linear model traces this limit almost exactly. The cosine model, which gives the highest incompleteness estimates, is most consistent with the lower boundary. We summarise the lower limit on the incompleteness in the last line of Table 4.

Note the tail of MCs at large ρ values identified in the additional data. There are a total of 10 MCs with $\rho > \rho_{\text{min}}$, however the tail consists mostly of six objects at $\rho > 0.45$ arcsec. Their large ρ values are due to r_e measurement errors caused by slightly

Table 4. Estimates of the MGC’s incompleteness due to misclassification of galaxies as stars ($16 \leq B_{\text{MGC}} < 20$ mag).

	$\rho_{\text{min}} < \rho$		$0 < \rho$		$0 < \rho < \rho_{\text{min}}$	
	$I_{\text{g}}(<)^a$	$R_{\text{g}}^b(<)^a$	$I_{\text{g}}(<)^a$	$R_{\text{g}}^b(<)^a$	$I_{\text{g}}(<)^a$	$R_{\text{g}}^b(<)^a$
	(per cent)		(per cent)		(per cent)	
From Section 4.1, using different models:						
Linear	0.05(0.51)	(0.41)	0.49(1.28)	0.02(0.81)	36.0(50.5)	5.2(26.7)
Gaussian	0.15(0.66)	0.05(0.56)	0.86(2.01)	0.39(1.54)	48.1(64.2)	23.2(47.0)
Cosine	0.07(0.51)	(0.41)	1.05(2.31)	0.58(1.85)	56.1(70.5)	35.0(56.4)
From Section 4.2, based on different objects:						
galaxies	0(0.52)	(0.42)	0.45(1.40)	(0.95)	35.8(52.8)	6.6(31.3)
stellar objects	0(0.93)	(0.83)	0.65(1.98)	0.19(1.52)	44.9(57.4)	19.8(38.0)
visually inspected	0(0.99)	(0.90)	1.07(2.94)	0.61(2.49)	57.1(71.5)	37.6(58.6)
Area	0(0.82)	(0.72)	0.54(1.69)	0.07(1.23)	41.4(53.8)	13.2(31.6)
From Section 4.3	0.14	0.04	0.61	0.15	38.6	9.0
Lower limit ^c	0.10		0.47		32.5	

^aUpper limit at 95 per cent confidence.

^bRemaining incompleteness after accounting for ‘real’ MCs already known.

^cDerived from all known ‘real’ MCs in the MGC.

erroneous SEXTRACTOR object ellipses which in turn are due to nearby bright objects in four of the six cases. The one-parameter models are not equipped to handle a non-zero tail of objects at large ρ . The gaussian is best suited, but even for this model the incompleteness derived from these objects eventually exceeds even the upper end of the 90 per cent confidence range. This highlights that the derived errors on the incompleteness estimates do not include the shortcomings of the chosen models.

In columns 3, 5 and 7 of Table 4 we list the MGC’s remaining incompleteness, $R_{\text{g}}(\rho_{\text{lim}})$, after accounting for those MCs that have already been discovered. Specifically, R_{g} is calculated by applying equation (9) after having subtracted the known ‘real’ MCs from the number of MCs predicted from the all-object region ($N_{\text{MC}}^{\text{MGC}}$) in the numerator. If the number of known MCs exceeds the predicted number (see discussion above) we only list an upper limit.

4.2 Assuming $\Gamma_{\text{AO}} = \Gamma_{\text{MGC}}$

Recall that the formalism of the previous Section was necessary because of the different seeing in the all-object region and the MGC as a whole. In this Section we will simply ignore this difference. Since in fact $\Gamma_{\text{AO}} < \Gamma_{\text{MGC}}$, this assumption introduces a bias towards lower incompleteness.

Ignoring the seeing difference means that we can assume that the ρ distribution of galaxies in the all-object region is the same as in the full MGC (apart from the normalisation):

$$n_{\text{G}}^{\text{AO}}(\rho) = n_{\text{G}}^{\text{MGC}}(\rho) \frac{N_{\text{G}}^{\text{AO}}}{N_{\text{G}}^{\text{MGC}}}, \quad (10)$$

where $N = \int_{-\infty}^{\infty} n(\rho) d\rho$. Substituting into equations (2) and (1) we find for the number of misclassified galaxies in the full MGC:

$$N_{\text{MC}}^{\text{MGC}}(\rho_{\text{lim}}) = N_{\text{MC}}^{\text{AO}}(\rho_{\text{lim}}) \frac{N_{\text{G}}^{\text{MGC}}}{N_{\text{G}}^{\text{AO}}}, \quad (11)$$

i.e. we simply scale the number of MCs in the all-object region by the ratio of the total numbers of galaxies in the full MGC and the all-object region. For simplicity and so that we do not have to make any reference to objects with $\rho < \rho_{\text{lim}}$ we prefer to replace this ratio with $N_{\text{G}}^{\text{MGC}}(\rho_{\text{lim}})/N_{\text{G}}^{\text{AO}}(\rho_{\text{lim}})$ which is valid under the assump-

tion of having the same seeing in the all-object region and in the full MGC. In analogy to equation (2) we now define the ‘cumulative’ binomial probability as

$$\tilde{p}_{\text{g}}(\rho_{\text{lim}}) = \frac{N_{\text{MC}}^{\text{AO}}(\rho_{\text{lim}})}{N_{\text{G}}^{\text{AO}}(\rho_{\text{lim}})} \quad (12)$$

and we rewrite equation (11) as

$$\begin{aligned} N_{\text{MC}}^{\text{MGC}}(\rho_{\text{lim}}) &= \tilde{p}_{\text{g}}(\rho_{\text{lim}}) N_{\text{G}}^{\text{MGC}}(\rho_{\text{lim}}) \\ &= \tilde{p}_{\text{g}}(\rho_{\text{lim}}) [N_{\text{MC}}^{\text{MGC}}(\rho_{\text{lim}}) + N_{\text{G}}^{\text{MGC}}(\rho_{\text{lim}})] \\ &= \frac{\tilde{p}_{\text{g}}(\rho_{\text{lim}})}{1 - \tilde{p}_{\text{g}}(\rho_{\text{lim}})} N_{\text{G}}^{\text{MGC}}(\rho_{\text{lim}}), \end{aligned} \quad (13)$$

analogous to equation (8).

Given the assumption $\Gamma_{\text{AO}} = \Gamma_{\text{MGC}}$ we can consider several other ways of estimating $N_{\text{MC}}^{\text{MGC}}$:

First, instead of scaling the number of MCs by the total number of galaxies as in equation (11), we can simply scale by the observed areas on the sky, A , thus making no reference to any objects other than the MCs:

$$N_{\text{MC}}^{\text{MGC}}(\rho_{\text{lim}}) = N_{\text{MC}}^{\text{AO}}(\rho_{\text{lim}}) \frac{A^{\text{MGC}}}{A^{\text{AO}}} \quad (14)$$

Next, from an a posteriori point of view it is interesting to ask: given an object morphologically classified as stellar, what is the binomial probability, \tilde{p}_{s} , that it is actually a galaxy? We now have

$$\tilde{p}_{\text{s}}(\rho_{\text{lim}}) = \frac{N_{\text{MC}}^{\text{AO}}(\rho_{\text{lim}})}{N_{\text{s}}^{\text{AO}}(\rho_{\text{lim}})} \quad (15)$$

and

$$N_{\text{MC}}^{\text{MGC}}(\rho_{\text{lim}}) = \tilde{p}_{\text{s}}(\rho_{\text{lim}}) N_{\text{s}}^{\text{MGC}}(\rho_{\text{lim}}), \quad (16)$$

where N_{s} is the number of objects morphologically classified as stellar. This includes stars, QSOs and MCs. Note that the process of testing whether a morphologically stellar object is in fact a galaxy is not really a binomial process because the outcome is pre-determined. In fact, compared to the previous two estimates of this Section we expect equation (16) to result in a higher incompleteness because the average stellar density in the full survey is higher than in the all-object region (due to different mean Galactic latitudes, cf. fig. 11 of Liske et al. 2003).

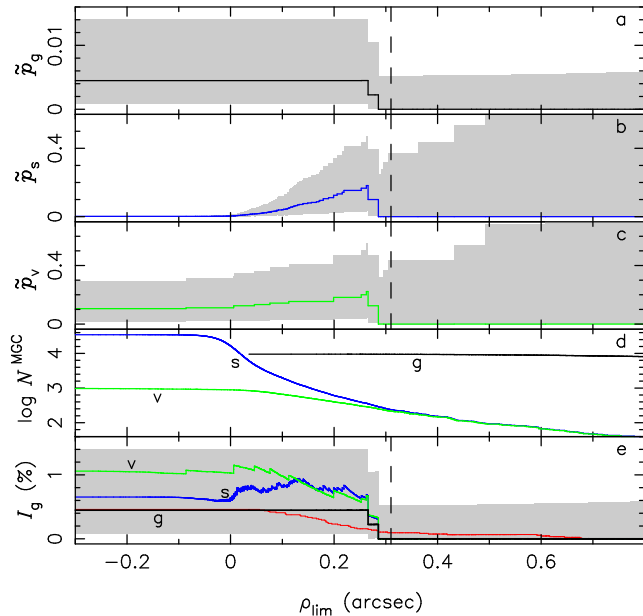


Figure 13. (a) Cumulative binomial probability of misclassifying a galaxy with $\rho > \rho_{\text{lim}}$ as a star. (b) Cumulative binomial probability that an object classified as stellar and with $\rho > \rho_{\text{lim}}$ is actually a galaxy. (c) Cumulative binomial probability that an object classified as stellar by visual inspection and with $\rho > \rho_{\text{lim}}$ is actually a galaxy. (d) Number of objects in the full MGC survey region with $\rho > \rho_{\text{lim}}$: ‘g’ and ‘s’ refer to objects originally classified as galaxies and stars, while ‘v’ denotes that subset of ‘s’ which was classified by eye. (e) Estimates of the incompleteness of galaxies with $\rho > \rho_{\text{lim}}$ due to their misclassification as stars based on the probabilities in panels (a)–(c) (which were derived from the all-object region) and the numbers of objects in panel (d) as indicated. The thin red line is the incompleteness derived from all known (‘real’) MCs in the full MGC survey region, and gives a lower limit on the true incompleteness. The grey shaded areas show 90 per cent confidence ranges and the vertical dashed line marks the minimum size limit adopted by Driver et al. (2005).

Finally, we note that both of the MCs in the all-object region have stellaricity < 0.98 (cf. Fig. 4) and therefore their original classification as stars was the result of visual inspection (see Section 2.1). Hence we can gain yet another estimate of the incompleteness by substituting N_s above with the respective number of stellar objects classified as such by visual inspection, N_v . However, we must expect this estimate to return an even higher incompleteness than the previous one because it suffers an additional bias: the fraction of stars classified visually is higher in the full survey than in the all-object region because of the worse seeing.

In Fig. 13 we show the above cumulative probabilities derived from the all-object region (panels a–c), the appropriate numbers of objects in the full survey region (d) and the resulting incompleteness estimates (e). The latter are summarised in Table 4.

Given the errors, the derived I_g values of this Section are reasonably consistent with each other. This implies that the effects of the differences in the stellar density and visually classified fraction between the all-object region and the full MGC are not dramatic. Nevertheless, they are detectable, and we have $I_g < I_g^s < I_g^v$ as expected. We also find that I_g is smaller than the incompleteness estimates from the previous Section and we attribute this to the seeing difference between the all-object region and the full MGC. However, compared to the size of the random errors the systematic shift is again small.

Note that both MCs in the all-object region have $\rho < \rho_{\text{min}}$.

Therefore the all-object region predicts $I_g(\rho_{\text{lim}} = \rho_{\text{min}}) = 0$ which is of course below the lower limit set by the sample of already known MCs in the full MGC (again shown as a thin red line in Fig. 13e). Hence, in Table 4 we only list upper limits for the residual incompleteness R_g at ρ_{min} .

A major difference between Figs. 13(e) and 12(d) is the size of the errors for large ρ_{lim} . The error of, say, $I_g(0.6)$ in Fig. 13(e) is simply set by the observation that none out of $N_g^{\text{MGC}}(0.6)$ galaxies in the all-object region had been misclassified, while the smallness of the error on $I_g^{\text{gaus}}(0.6)$ in Fig. 12(d) is due to the additional assumption of a specific function for p_g .

Even though $I_g(\rho_{\text{lim}})$ should be a monotonic function, I_g^s in Fig. 13(e) exhibits a small decline from $\rho_{\text{lim}} \approx 0.12$ to 0 arcsec. This reflects a small misalignment between the stellar ρ distributions, $n_s(\rho)$, in the all-object region and the full survey. In any case, since the fluctuation is much smaller than the errors, it has little effect on the result.

4.3 Correcting the MC sample for incompleteness

In the bottom panels of Figs. 12 and 13 we have compared the various I_g estimates predicted from the *complete* sample of MCs in the all-object region with the lower limit on I_g derived from the *incomplete* sample of all known ‘real’ MCs in the full MGC. Almost all of the estimates are within a factor of 2 of the lower limit, suggesting that our additional observations of stellar objects have probed at least part of that region of observational parameter space in which MCs exist.

As a cross-check we will now apply a rudimentary correction to the number of MCs discovered outside of the all-object region (see Section 2.2.2) to see whether we recover a similar overall incompleteness as in the previous Sections. We perform the correction by dividing the four-dimensional parameter space spanned by B_{MGC} , $(u - g)$, $(g - z)$ and SDSS-DR1 morphological classification into five separate regions. We then determine the spectroscopic incompleteness of stellar objects in each of these regions and apply this factor to the number of MCs discovered in them, implicitly assuming that each region was sampled homogeneously. Since MGCz contributed most of the spectra in the ‘additional’ sample, we follow the MGCz target selection described in Section 2.2.2 in defining the above regions. The result of applying this correction is that the MGC’s overall incompleteness is 0.61 per cent, in reasonable agreement with the models of Section 4.1 (cf. column 4 of Table 4). The 95 per cent confidence upper limit on this number is 1.74 per cent but there is an unknown additional uncertainty due to our use of an approximate selection function. Hence the estimate above is much less reliable than those of the previous Sections and we do not quote any upper limits in Table 4.

5 LUMINOSITY FUNCTION AND DENSITY INCLUDING COMPACT GALAXIES

In the previous Section we have seen that the standard MGC galaxy catalogue is missing up to 64 per cent of galaxies with $r_e < r_{\text{min}}$. However, since this translates to only 2 per cent of *all* galaxies (cf. columns 6 and 4 of Table 4, gaussian model) one might be tempted to conclude that MCs and other compact galaxies are entirely negligible with respect to the galaxy population as a whole. However, since the raw number of non-compact galaxies is dominated by luminous objects and since compact galaxies are preferentially faint (cf. right panel of Fig. 9), the above impression may be misleading.

Clearly, we need to consider the issue as a function of luminosity before we can reach a final conclusion regarding the relevance of compact galaxies and their misclassification. The goal of this Section is therefore to evaluate the contribution of compact galaxies to the local galaxy LF.

In the following we construct LFs using a variant of the bivariate step-wise maximum likelihood (SWML) method of Driver et al. (2005). We impose the same apparent magnitude, low-SB and redshift limits: $13 < B_{\text{MGC}} < 20$ mag, $r_e < 15$ arcsec, $\mu_{\text{eff}} < 25.25$ mag arcsec $^{-2}$ and $0.013 < z < 0.18$, but we do *not* impose a minimum size limit. In our context of compact galaxies we can hence regard this method as being equivalent to a standard mono-variate SWML analysis (Efstathiou, Ellis & Peterson 1988), where all SB selection effects are ignored. The only difference is that we are in fact accounting for the MGC's low-SB limits.

The application of the above limits leaves us with 7803 non-misclassified galaxies. To convert apparent to absolute magnitudes we use the Driver et al. global evolutionary correction and individual K -corrections, where the former is given by $E(z) = -0.75 \times 2.5 \log(1+z)$.

We begin now by first constructing the LF of non-compact galaxies only, i.e. we exclude all MCs as well as all non-misclassified galaxies with $r_e < r_{\text{min}}$ from the sample. This is the sample that would result from a severe high-SB selection effect (in the sense that *every* galaxy below r_{min} is missed) and its LF will obviously be an under-estimate of the true LF. In the following we will refer to this as the non-compact LF (NCLF). In Fig. 14 we show the NCLF as black solid squares, where we have normalised all data points by an arbitrarily chosen Schechter (1976) function with parameters: $M_B^* - 5 \log h = -19.63$ mag, $\phi^* = 0.0174 h^3 \text{ Mpc}^{-3}$ and $\alpha = -1.16$. We show only poisson errors since we will only be comparing various estimates of the LF derived from essentially the same volume.

Next we add in the non-misclassified compact galaxies with $r_e < r_{\text{min}}$ (CGs), which somewhat raises the LF at the faint end as expected (blue open squares). However, we know that these CGs are ~ 50 per cent incomplete, and so we are still under-estimating the true LF. This is the LF one obtains from the MGC data if the issue of high-SB selection effects is simply ignored.

The brown open circles in Fig. 14 show the result of also adding in the known 'real' MCs. Since not all MCs were actually discovered, this sample is still incomplete and we are still under-estimating the true LF.

Finally, we derive a LF estimate using an incompleteness correction: in Section 4.1 we postulated that the classification of galaxies is a random process, where the binomial probability of misclassifying a galaxy as a star, p_g , depends only on the galaxy's $\rho = r_e - 0.6 \Gamma$. Hence we can recover the total number of galaxies by simply weighting each non-misclassified galaxy by $[1 - p_g(\rho)]^{-1}$. The result is shown as red solid dots in Fig. 14 where we have used the gaussian estimate of p_g (cf. Section 4.1). Using the cosine or linear estimates instead results in the LFs marked by the upper and lower ends of the light red vertical boxes respectively. The errorbars protruding from these boxes show the uncertainties due to the 90 percentile errors on the cosine and linear model parameters.

We list the parameters of the best fitting Schechter functions of the above LFs in Table 5.

For comparison we also plot in Fig. 14 as green open triangles the MGC LF as derived by using the fully bivariate SWML method of Driver et al. (2005), including the minimum size limit. In this case we are using the same sample as for the NCLF, i.e. the MCs and CGs are excluded, but now the r_{min} selection limit is properly

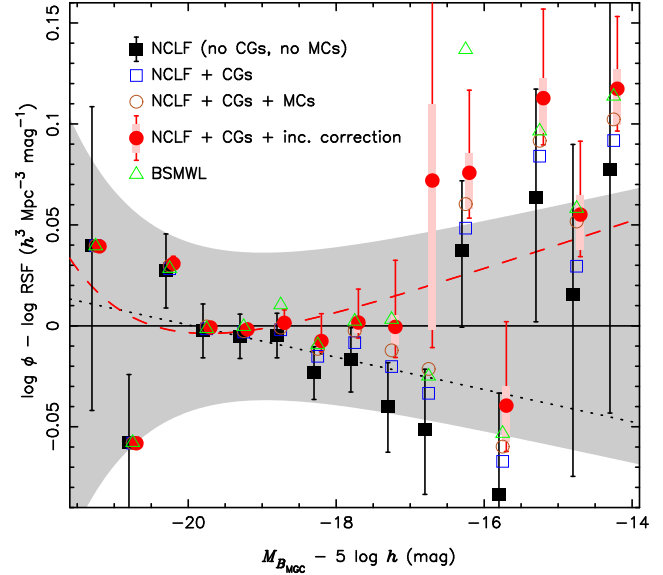


Figure 14. Various estimates of the MGC's luminosity function as indicated and explained in the text. All estimates are normalised by an arbitrary reference Schechter function (RSF), which has $M_B^* - 5 \log h = -19.63$ mag, $\phi^* = 0.0174 h^3 \text{ Mpc}^{-3}$ and $\alpha = -1.16$. The grey shaded area shows a $\pm 1\sigma$ range around the RSF that is typical of the Schechter function fits of the various LFs. The LFs are derived using an essentially standard SWML method, except the one labelled 'BSMWL' where we use the full bivariate method of Driver et al. (2005). 'CGs' refers to non-misclassified compact galaxies. The errors on the NCLF are poissonian only. The errors on the incompleteness corrected LF reflect the uncertainties due to the choice of the incompleteness model (boxes) and the models' parameters (errorbars). The black dotted and red dashed lines show the best fit Schechter function for the NCLF and the incompleteness corrected LF respectively. Some data points are offset horizontally for clarity.

taken into account in the SWML analysis by appropriately reducing each galaxy's observable parameter space in the luminosity–SB plane. This is equivalent to reducing the volume over which a galaxy could have been observed, and hence the resulting LF is somewhat higher than in the standard NCLF case.

Examining Fig. 14 we first of all notice that measurable differences between the various LF estimates are confined to the regime $M_B \gtrsim -18$ mag. As mentioned above, this is due to the combined effect of r_{min} and the luminosity–size relation of galaxies as discussed in connection with Fig. 10.

Secondly, comparing the red dots to the blue open squares, it seems that the incompleteness of compact galaxies due to misclassification does not affect the LF significantly: for almost all points the differences are smaller than the 1σ poisson error. In this sense even the effect of the *total* compact galaxy population is only marginally significant (comparing the red dots with the black squares). However, the impact of the compact galaxies is obviously systematic and hence more significant when considering the faint end of the LF as a whole: the overall effect of the compact galaxies is to steepen the faint-end slope α by 0.05, which is a 2.5σ effect (cf. Table 5), while the misclassified galaxies alone steepen α by 0.03, which is still marginally significant. The steepening increases to 0.05 if we use the upper end of the 90 percentile confidence range on $p_g^{\text{aus}}(\rho)$, and to 0.06 if we use the most extreme incompleteness correction (cf. last line of Table 5).

To further illustrate this point, we directly compare the LFs of compact and non-compact galaxies in absolute terms in Fig. 15.

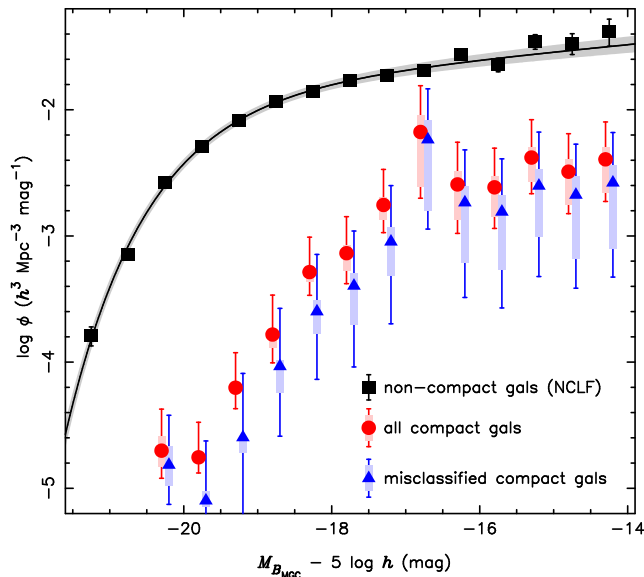


Figure 15. LFs of compact and non-compact galaxies as indicated. The black line and grey region show the Schechter function that best fits the NCLF, and $\pm 1\sigma$ range. All errorbars have the same meaning as in Fig. 14.

Although there are ~ 2 orders of magnitude fewer compact galaxies than non-compact ones at bright magnitudes, they make up ~ 10 per cent of all galaxies in the range $-17 < M_B < -14$ mag, and the misclassified galaxies alone contribute ~ 6 per cent in this range.

Finally, comparing the incompleteness corrected LF to the fully bivariate SWML estimate in Fig. 14 (green triangles) we find that the two agree very well for almost all points. Put simply, the first method corrects for missing objects while the second method corrects for missing parameter space (or volume), and it is reassuring that the two methods yield the same result with no obvious systematic bias.

Since the luminosity density, j , is dominated by the bright end of the LF it is only marginally affected by the compact galaxies. For a given LF we calculate the luminosity density from the parameters of the best fit Schechter function as $j = \phi^* L_{B_{MGC}}^* \Gamma(\alpha + 2)$. From the last column of Table 5 we can see that the inclusion of compact galaxies increases j by 3.5 per cent, while the misclassified galaxies alone are responsible for an increase of only 2 per cent.

6 CONCLUSIONS

We have explored the very high surface brightness (SB) regime of the Millennium Galaxy Catalogue (MGC) to assess the impact of compact galaxies on the field galaxy luminosity function (LF) in the local ($z \approx 0.1$) Universe. We have observationally defined ‘compact galaxies’ as objects whose half light-radii are so small that they cannot *reliably* be distinguished from stars in the MGC using SExtractor and/or visual examination (i.e. $r_e \lesssim 1$ arcsec).

We have studied the incompleteness of the standard MGC galaxy catalogue ($B_{MGC} < 20$ mag) due to the misclassification of compact galaxies as stars using the 1.14 deg^2 all-object sub-region of the MGC, where we have spectroscopically identified *all* galaxies in the range $16 < B_{MGC} < 20$ mag. We find:

1. Within the MGC’s minimum size limit (as derived by Driver et al. 2005) only 0.15 per cent of galaxies are missed due to their compactness, with a 95 per cent upper limit of 0.66 per

cent. Hence we verify Driver et al.’s assumption that the MGC is complete within its minimum size limit.

2. Beyond the minimum size limit ~ 50 per cent of galaxies are misclassified as stars.

3. However, with respect to the total galaxy population this translates to an incompleteness of only 1.05 per cent of all galaxies, with a 95 per cent upper limit of 2.31 per cent.

Our incompleteness is a factor of 2.6 lower than the (2.8 ± 1.6) per cent found by Drinkwater et al. (1999) for galaxies with $16.5 \leq b_J \leq 19.7$ mag in the Fornax Cluster Spectroscopic Survey (FCSS). This is presumably due to the higher resolution of the MGC compared to the UK Schmidt photographic data from which the FCSS was selected. The null-result of Morton et al. (1985) on the other hand can be explained by their small survey area of 0.31 deg^2 .

The incompleteness values above ignore the fact that a total of 47 misclassified compact galaxies (MCs) have already been discovered through additional spectroscopy of morphologically stellar objects. Accounting for these objects reduces the overall incompleteness to just 0.58 per cent.

Using this extended, albeit incomplete sample of 47 objects we have studied the nature of the MCs. Over 90 per cent of them are emission line galaxies (similar to the fraction of Drinkwater et al. 1999), but we also find three E+A galaxies. Although some E+A show clear signs of interaction (Zabludoff et al. 1996; Yang et al. 2004) they are generally found to be bulge-dominated, spheroidal systems (Quintero et al. 2004; Yang et al. 2004; Blake et al. 2004) with bright compact cores (Goto 2005) and higher central SB than normal bulge-dominated galaxies (Quintero et al. 2004; Yang et al. 2004). Hence their appearance among the MCs is not too surprising.

An analysis of emission line ratios revealed that four of the emission line galaxies harbour a type 2 AGN. Even though early studies of Seyfert galaxies seemed to suggest that they were mostly hosted by spiral galaxies (Adams 1977), recent results from the SDSS have shown that the surface mass density distribution of type 2 AGN hosts is very similar to that of normal early-type galaxies (Kauffmann et al. 2003a). Also, their concentration index distribution extends to very high values and so we conclude that our compact type 2s are not unusual.

Blue compact galaxies, although ill-defined, are the most common and widely studied class of compact galaxies (see Kunth & Östlin 2000 for a review) and we find that 83 per cent of our MCs are blue, star-forming galaxies with strong nebular emission lines. We note that these galaxies generally have $M_B > -19$ mag and are hence fainter than the luminous blue compact galaxies (e.g. Phillips et al. 1997; Werk et al. 2004) but overlap with the blue compact dwarfs (BCDs; e.g. Thuan & Martin 1981; Gil de Paz et al. 2003).

The ‘blue spheroids’ of Ellis et al. (2005) (see also Cross et al. 2004; Driver et al. 2006) are another type of blue, star-forming, sub- L^* galaxy. However, in contrast to the BCDs, which often have disturbed or irregular morphologies (Cairós et al. 2001), the blue spheroids are very smooth, with concentration and asymmetry indices similar to normal ellipticals. Since our MCs are only barely resolved we have not been able to reliably fit their SB profiles. Hence, without higher resolution imaging it is not possible to decide whether the MCs are more similar to BCDs or a high SB version of the blue spheroids.

The faintness of the MCs, which is essentially due to the luminosity–size relation of galaxies, is the cause of their differential effect on the local galaxy luminosity function: our main re-

Table 5. Schechter function parameters for the LFs of Fig. 14.

Sample	ϕ^* ($10^{-2}h^3 \text{ Mpc}^{-3}$)	$M_B^* - 5 \log h$ (mag)	α	j ($10^8 h L_\odot \text{ Mpc}^{-3}$)
NCLF	1.73 ± 0.07	-19.63 ± 0.04	-1.14 ± 0.02	1.93 ± 0.13
NCLF+CGs	1.72	-19.64	-1.16	1.97
NCLF+CGs+MCs	1.70	-19.64	-1.17	1.96
NCLF+CGs+inc. correction	1.67	-19.66	-1.19	2.00
NCLF+CGs+extreme inc. cor. ^a	1.64	-19.68	-1.22	2.06

^aUsing the upper end of the 90 percentile confidence range of the cosine estimate of $p_g(\rho)$.

sult is that even in the relatively high-resolution MGC the misclassification of compact galaxies as stars causes the LF to be systematically underestimated at the faint end by $\Delta\alpha = 0.03_{-0.01}^{+0.02}$, while the bright end remains unaffected. The faint-end bias is comparable in size to the poisson errors of the MGC and misclassified galaxies contribute ~ 6 per cent to the LF in the range $-17 < M_B < -14$ mag. In contrast, the luminosity density is only affected at the ~ 2 per cent level.

Clearly, we have *not* uncovered a large population of galaxies ‘hiding’ among the stars. On the other hand, high-SB selection effects are not completely negligible either and hence should be taken into account when constructing LFs. This is ‘naturally’ achieved by first constructing the bivariate space density of galaxies in either the luminosity–SB or luminosity–size plane using a bivariate SWML method, and then integrating over the second parameter to obtain the LF (Driver et al. 2005). Here we have confirmed that this method recovers a result very close to an incompleteness corrected LF.

Our result regarding the *high* SB end of the galaxy distribution should be viewed together with the situation at the *low* SB end. While *luminous* galaxies are not affected by low SB selection effects (e.g. Driver et al. 2005), *faint* galaxies are. Blanton et al. (2005) recently presented an SDSS LF corrected for low SB incompleteness at $\mu_{\text{eff},r} \gtrsim 23$ mag arcsec $^{-2}$ and concluded that the correction resulted in a significant steepening of the faint end of the LF. Indeed, at $M_B \gtrsim -16$ mag the galaxy population extends to even the deeper MGC’s SB limit of $\mu_{\text{lim}} = 25.25$ mag arcsec $^{-2}$ (Driver et al. 2005). Hence, even in the MGC the faint end of the LF is significantly affected by both low and high SB selection effects, despite the fact that the MGC is both deeper and of higher resolution than any previous major ground-based survey. Clearly, to obtain a complete view of the dwarf galaxy population requires still deeper and higher resolution imaging (soon to be delivered by the VLT Survey Telescope) as well as spectroscopy on 8-m class telescopes.

ACKNOWLEDGMENTS

The Millennium Galaxy Catalogue consists of imaging data from the Isaac Newton Telescope and spectroscopic data from the Anglo Australian Telescope, the ANU 2.3m, the ESO New Technology Telescope (73.A-0092), the Telescopio Nazionale Galileo, and the Gemini Telescope. The survey has been supported through grants from the Particle Physics and Astronomy Research Council (UK) and the Australian Research Council (AUS). The data and data products are publicly available from <http://www.eso.org/~jliske/mgc/> or on request from JL or SPD.

Funding for the creation and distribution of the SDSS Archive

has been provided by the Alfred P. Sloan Foundation, the Participating Institutions, the National Aeronautics and Space Administration, the National Science Foundation, the U.S. Department of Energy, the Japanese Monbukagakusho, and the Max Planck Society. The SDSS Web site is <http://www.sdss.org/>. The SDSS is managed by the Astrophysical Research Consortium (ARC) for the Participating Institutions. The Participating Institutions are The University of Chicago, Fermilab, the Institute for Advanced Study, the Japan Participation Group, The Johns Hopkins University, the Korean Scientist Group, Los Alamos National Laboratory, the Max-Planck-Institute for Astronomy (MPIA), the Max-Planck-Institute for Astrophysics (MPA), New Mexico State University, University of Pittsburgh, Princeton University, the United States Naval Observatory, and the University of Washington.

REFERENCES

- Abazajian K., et al., 2003, AJ, 126, 2081
Adams T. F., 1977, ApJS, 33, 19
Anderson S. F., et al., 2003, AJ, 126, 2209
Arp H., 1965, ApJ, 142, 402
Baldry I. K., Glazebrook K., Brinkmann J., Ivezić Ž., Lupton R. H., Nichol R. C., Szalay A. S., 2004, ApJ, 600, 681
Baldwin J. A., Phillips M. M., Terlevich R., 1981, PASP, 93, 5
Balogh M. L., Miller C., Nichol R., Zabludoff A., Goto T., 2005, MNRAS, 360, 587
Bertin E., Arnouts S., 1996, A&AS, 117, 393
Blake C., et al., 2004, MNRAS, 355, 713
Blanton M. R., Lupton R. H., Schlegel D. J., Strauss M. A., Brinkmann J., Fukugita M., Loveday J., 2005, ApJ, 631, 208
Bothun G. D., Impey C. D., Malin D. F., Mould J. R., 1987, AJ, 94, 23
Brinchmann J., Charlot S., White S. D. M., Tremonti C., Kauffmann G., Heckman T., Brinkmann J., 2004, MNRAS, 351, 1151
Cairós L. M., Vílchez J. M., González Pérez J. N., Iglesias-Páramo J., Caon N., 2001, ApJS, 133, 321
Cid Fernandes R., Heckman T., Schmitt H., Delgado R. M. G., Storchi-Bergmann T., 2001, ApJ, 558, 81
Colless M., Ellis R. S., Shaw G., Taylor K., 1991, MNRAS, 253, 686
Colless M., Ellis R. S., Taylor K., Hook R. N., 1990, MNRAS, 244, 408
Colless M., et al., 2001, MNRAS, 328, 1039
Croom S. M., Smith R. J., Boyle B. J., Shanks T., Miller L., Outram P. J., Loaring N. S., 2004, MNRAS, 349, 1397
Cross N. J. G., Driver S. P., Liske J., Lemon D. J., Peacock J. A., Cole S., Norberg P., Sutherland W. J., 2004, MNRAS, 349, 576
Cross N. J. G., et al., 2004, AJ, 128, 1990

- de Vries W. H., Becker R. H., White R. L., 2003, *AJ*, 126, 1217
- Disney M. J., 1976, *Nat*, 263, 573
- Dressler A., Gunn J. E., 1983, *ApJ*, 270, 7
- Drinkwater M. J., et al., 2000, *A&A*, 355, 900
- Drinkwater M. J., Gregg M. D., Hilker M., Bekki K., Couch W. J., Ferguson H. C., Jones J. B., Phillipps S., 2003, *Nat*, 423, 519
- Drinkwater M. J., Jones J. B., Gregg M. D., Phillipps S., 2000, *PASP*, 17, 227
- Drinkwater M. J., Phillipps S., Gregg M. D., Parker Q. A., Smith R. M., Davies J. I., Jones J. B., Sadler E. M., 1999, *ApJ*, 511, L97
- Driver S. P., et al., 2006, *MNRAS*, in press, astro-ph/0602240
- Driver S. P., Liske J., Cross N. J. G., De Propriis R., Allen P. D., 2005, *MNRAS*, 360, 81
- Efstathiou G., Ellis R. S., Peterson B. A., 1988, *MNRAS*, 232, 431
- Ellis S. C., Driver S. P., Allen P. D., Liske J., Bland-Hawthorn J., De Propriis R., 2005, *MNRAS*, 363, 1257
- Francis P. J., 1993, *ApJ*, 407, 519
- Gil de Paz A., Madore B. F., Pevunova O., 2003, *ApJS*, 147, 29
- Goto T., 2005, *MNRAS*, 357, 937
- Guzman R., Jangren A., Koo D. C., Bershady M. A., Simard L., 1998, *ApJ*, 495, L13
- Guzman R., Koo D. C., Faber S. M., Illingworth G. D., Takamiya M., Kron R. G., Bershady M. A., 1996, *ApJ*, 460, L5
- Guzmán R., Östlin G., Kunth D., Bershady M. A., Koo D. C., Pahre M. A., 2003, *ApJ*, 586, L45
- Hambly N. C., et al., 2001, *MNRAS*, 326, 1279
- Haşegan M., et al., 2005, *ApJ*, 627, 203
- Hilker M., Infante L., Vieira G., Kissler-Patig M., Richtler T., 1999, *A&AS*, 134, 75
- Ho L. C., Filippenko A. V., Sargent W. L. W., 1993, *ApJ*, 417, 63
- Impey C., Bothun G., 1997, *ARA&A*, 35, 267
- Kauffmann G., et al., 2003a, *MNRAS*, 346, 1055
- Kauffmann G., et al., 2003b, *MNRAS*, 341, 33
- Kewley L. J., Dopita M. A., Sutherland R. S., Heisler C. A., Trevena J., 2001, *ApJ*, 556, 121
- Kniazev A. Y., Pustilnik S. A., Grebel E. K., Lee H., Pramskij A. G., 2004, *ApJS*, 153, 429
- Koo D. C., Bershady M. A., Wirth G. D., Stanford S. A., Majewski S. R., 1994, *ApJ*, 427, L9
- Koo D. C., Guzman R., Faber S. M., Illingworth G. D., Bershady M. A., Kron R. G., Takamiya M., 1995, *ApJ*, 440, L49
- Kunth D., Östlin G., 2000, *A&AR*, 10, 1
- Liske J., Lemon D. J., Driver S. P., Cross N. J. G., Couch W. J., 2003, *MNRAS*, 344, 307
- Londish D., et al., 2002, *MNRAS*, 334, 941
- Mieske S., et al., 2004, *AJ*, 128, 1529
- Mieske S., Hilker M., Infante L., 2004, *A&A*, 418, 445
- Monet D. G., et al., 2003, *AJ*, 125, 984
- Morton D. C., Krug P. A., Tritton K. P., 1985, *MNRAS*, 212, 325
- Phillips A. C., Guzman R., Gallego J., Koo D. C., Lowenthal J. D., Vogt N. P., Faber S. M., Illingworth G. D., 1997, *ApJ*, 489, 543
- Quintero A. D., et al., 2004, *ApJ*, 602, 190
- Reaves G., 1956, *AJ*, 61, 69
- Richards G. T., et al., 2001, *AJ*, 121, 2308
- Richards G. T., et al., 2003, *AJ*, 126, 1131
- Sargent W. L. W., Searle L., 1970, *ApJ*, 162, L155
- Schechter P., 1976, *ApJ*, 203, 297
- Schmitt H. R., Storchi-Bergmann T., Fernandes R. C., 1999, *MNRAS*, 303, 173
- Schneider D. P., et al., 2003, *AJ*, 126, 2579
- Schneider D. P., et al., 2005, *AJ*, 130, 367
- Schwope A., et al., 2000, *Astron. Nachr.*, 321, 1
- Simpson C., 2005, *MNRAS*, 360, 565
- Storchi-Bergmann T., Raimann D., Bica E. L. D., Fraquelli H. A., 2000, *ApJ*, 544, 747
- Telles E., Melnick J., Terlevich R., 1997, *MNRAS*, 288, 78
- Thuan T. X., Martin G. E., 1981, *ApJ*, 247, 823
- Tremonti C. A., et al., 2004, *ApJ*, 613, 898
- Veilleux S., Osterbrock D. E., 1987, *ApJS*, 63, 295
- Voges W., et al., 1999, *A&A*, 349, 389
- Voges W., et al., 2000, *IAU Circ.*, 7432, 3
- Wagner S. J., Witzel A., 1995, *ARA&A*, 33, 163
- Werk J. K., Jangren A., Salzer J. J., 2004, *ApJ*, 617, 1004
- Wesemael F., Greenstein J. L., Liebert J., Lamontagne R., Fontaine G., Bergeron P., Glaspey J. W., 1993, *PASP*, 105, 761
- White R. L., Becker R. H., Helfand D. J., Gregg M. D., 1997, *ApJ*, 475, 479
- Williams R. J., Pogge R. W., Mathur S., 2002, *AJ*, 124, 3042
- Yang Y., Zabludoff A. I., Zaritsky D., Lauer T. R., Mihos J. C., 2004, *ApJ*, 607, 258
- York D. G., et al., 2000, *AJ*, 120, 1579
- Zabludoff A. I., Zaritsky D., Lin H., Tucker D., Hashimoto Y., Shectman S. A., Oemler A., Kirshner R. P., 1996, *ApJ*, 466, 104
- Zwicky F., 1957, *Morphological astronomy*. Springer, Berlin
- Zwicky F., 1966, *ApJ*, 143, 192